Disporum cantoniense suppresses non-small cell lung cancer through AMPK/mTOR/ULK1-mediated autophagy-dependent apoptosis

CHI FENG[1,2*], YUJIAO JI[3*], RENQIANG CHEN[4*], QIUXU CHEN[5*], YIRU PAN[3], JIANMING WU[3], DALIAN QIN[3], BETTY YUEN KWAN LAW[6], VINCENT KAM WAI WONG[6], XIAOGANG ZHOU[3], JIANXIN LIU[2] and ANGUO WU[3,7]

[1]Department of Pharmacy, Suining Chuanshan Hospital of Traditional Chinese Medicine, Sichuan 629000, P.R. China; [2]School of Pharmaceutical Sciences, Sino-Pakistan Center on Traditional Chinese Medicine, China-Pakistan International Science and Technology Innovation Cooperation Base for Ethnic Medicine Development in Hunan Province, Hunan University of Medicine, Huaihua, Hunan 418000, P.R. China; [3]Sichuan Key Medical Laboratory of New Drug Discovery and Druggability Evaluation, Luzhou Key Laboratory of Activity Screening and Druggability Evaluation for Chinese Materia Medica, Key Laboratory of Medical Electrophysiology of Ministry of Education, School of Pharmacy, Southwest Medical University, Luzhou, Sichuan 646000, P.R. China; [4]Department of Pharmacy, The Affiliated Hospital of Southwest Medical University, Luzhou, Sichuan 646000, P.R. China; [5]Department of Pharmacy, Ziyang Central Hospital, Ziyang, Sichuan 641300, P.R. China; [6]State Key Laboratory of Quality Research in Chinese Medicine, Macau University of Science and Technology, Taipa, Macau 999078, P.R. China; [7]Institute of Traditional Chinese Medicine Health Industry, China Academy of Chinese Medical Sciences, Nanchang 330115, P.R. China

Received May 15, 2026; Accepted August 27, 2026

DOI: 10.3892/ijo.2026.5950

Abstract. Non-small cell lung cancer (NSCLC) remains a leading cause of cancer-associated mortality and urgently requires new therapeutic agents. In the present study, phenotypic screening of natural herbal extracts was performed, identifying *Disporum cantoniense* extract as a selective inhibitor of NSCLC cell viability. Bioactivity-guided fractionation further revealed that the petroleum ether fraction (DPF) was the major active fraction. DPF suppressed the viability, proliferation, colony formation, migration and invasion of A549 and H1299 cells while exhibiting weaker cytotoxicity toward BEAS-2B cells. In addition, DPF increased propidium iodide (PI)-positive cell death and lactate dehydrogenase release in NSCLC cells, indicating that DPF-induced viability loss was accompanied by membrane-damaging cytotoxicity. Transcriptomic and network pharmacology analyses indicated significant enrichment of autophagy-, apoptosis-, AMPK-, mTOR-, and MAPK-associated pathways. Mechanistically, DPF increased LC3-II accumulation, promoted green fluorescent protein-LC3 puncta formation and autophagic flux, and activated the AMPK/mTOR/unc-51 like autophagy activating kinase 1 and MEK/ERK signaling pathways. DPF also induced apoptosis, as demonstrated by increased Annexin V positivity, elevated cleaved caspase-3 and Bax expression, reduced Bcl-2 expression, and reduced cytotoxicity in

Correspondence to: Professor Anguo Wu, Sichuan Key Medical Laboratory of New Drug Discovery and Druggability Evaluation, Luzhou Key Laboratory of Activity Screening and Druggability Evaluation for Chinese Materia Medica, Key Laboratory of Medical Electrophysiology of Ministry of Education, School of Pharmacy, Southwest Medical University, 319 Section 3, Zhongshan Road, Jiangyang, Luzhou, Sichuan 646000, P.R. China
E-mail: wuanguo1114@swmu.edu.cn

Professor Jianxin Liu, School of Pharmaceutical Sciences, Sino-Pakistan Center on Traditional Chinese Medicine, China-Pakistan International Science and Technology Innovation Cooperation Base for Ethnic Medicine Development in Hunan Province, Hunan University of Medicine, 492 Jinxi South Road, Huaihua, Hunan 418000, P.R. China
E-mail: jxliu@hnmu.edu.cn

*Contributed equally

Abbreviations: CC, compound C; CQ, chloroquine; DAD, diode-array detector; DE, *Disporum cantoniense* extract; DEF, *Disporum cantoniense* ethyl acetate fraction; DEGs, differentially expressed genes; DKO, double knockout; DNF, *Disporum cantoniense* n-butanol fraction; DPF, *Disporum cantoniense* petroleum ether fraction; DWF, *Disporum cantoniense* aqueous fraction; Gefi, gefitinib; GO, Gene Ontology; KEGG, Kyoto Encyclopedia of Genes and Genomes; MEF, mouse embryonic fibroblast; NSCLC, non-small cell lung cancer; PCA, principal component analysis; Rap, rapamycin; SCH, SCH772984; UHPLC-Q/TOF-MS/MS, ultra-high-performance liquid chromatography quadrupole time-of-flight tandem mass spectrometry; ZVF, Z-VAD-FMK; 3-MA, 3-methyladenine

Key words: Disporum cantoniense, non-small cell lung cancer, autophagy, apoptosis, AMPK/mTOR/unc-51 like autophagy activating kinase 1, MEK/ERK

Bax-Bak double-knockout mouse embryonic fibroblast (MEF) cells. Notably, pharmacological inhibition of autophagy or its upstream regulators attenuated DPF-induced cytotoxicity. In addition, autophagy-deficient Atg7$^{-/-}$ MEF cells exhibited reduced DPF-induced PI-positive cell death, loss of cell viability, and caspase-3 activation, further supporting the involvement of Atg7-dependent autophagy in DPF-induced apoptosis. In a xenograft model, DPF significantly inhibited tumor growth and increased apoptosis- and autophagy-associated markers in tumor tissues without evident systemic toxicity. Collectively, these findings identify DPF as a principal anti-NSCLC fraction of *Disporum cantoniense* and suggest that it suppresses NSCLC progression through AMPK/mTOR/unc-51 like autophagy activating kinase 1- and MEK/ERK-mediated autophagy-dependent apoptosis.

Introduction

Lung cancer remains a leading cause of cancer-associated mortality worldwide. According to GLOBOCAN 2022, there were ~2.5 million new lung cancer cases and >1.8 million deaths globally, underscoring the persistent and notable health burden imposed by this disease. Non-small cell lung cancer (NSCLC) accounts for ~80-85% of all lung cancers and therefore represents a dominant clinical and biological form of lung malignancy (1-3). Over the past decade, the treatment landscape of NSCLC has been transformed by molecular stratification, targeted therapy, and immune checkpoint blockade (4-8). Therapies targeted against actionable oncogenic drivers and immunotherapy-based regimens have markedly improved outcomes in selected patient subsets, such as patients with EGFR mutations or ALK rearrangements and those with high PD-L1 expression (9). However, these advances have not eliminated the major barriers to durable disease control, as intrinsic and acquired resistance, tumor plasticity, and metastatic progression continue to limit long-term benefits. Thus, despite therapeutic progress, advanced NSCLC remains associated with poor prognosis and a notable unmet clinical need (10-13).

A key challenge in NSCLC therapy is that malignant progression is driven not solely by uncontrolled proliferation but also by the ability of tumor cells to evade cell death and acquire invasive capacity. These hallmarks sustain tumor expansion, dissemination, and therapeutic failure. Agents capable of simultaneously suppressing proliferation, promoting tumor cell death, and attenuating invasion are therefore of marked interest in anticancer drug discovery, particularly when they act through multi-target or pathway-integrated mechanisms (11,14). Natural products have historically provided an important foundation for anticancer drug development, and recent advances in screening, analytical chemistry and mechanism-guided pharmacology, such as high-throughput screening, mechanistic pathway profiling, metabolic and redox target identification, and randomized controlled trials, have renewed interest in natural product-based drug discovery (15-18). The structural diversity and broad biological activity of natural products make them especially attractive as sources of lead compounds capable of modulating complex cancer phenotypes (19,20). In this context, activity-guided screening of medicinal plants remains a productive strategy for identifying candidate agents against NSCLC (21).

Disporum cantoniense is a medicinal plant with a history of traditional use and a growing phytochemical profile. Previous studies have identified flavonoids and other constituents from this species, and phytochemical investigations have reported compounds with anti-inflammatory potential (22,23). In addition, flavonoid-rich plant extracts have been widely reported to exhibit anti-tumor activities through modulation of apoptosis, oxidative stress, and metastasis-related pathways (16,24,25). These findings suggest that *Disporum cantoniense* contains bioactive small molecules with pharmacological relevance. However, its anti-tumor activity, particularly in NSCLC, has not been systematically investigated. To date, studies on *D. cantoniense* have mainly focused on its traditional anti-inflammatory applications and phytochemical characterization, whereas its oncology-related pharmacological effects remain largely unexplored. In addition, the specific bioactive fraction responsible for potential anti-NSCLC effects remains unidentified, and the underlying mechanisms of action are largely unknown. It remains unclear whether *Disporum cantoniense*-derived extracts or fractions selectively inhibit NSCLC cells, which fraction contains the major anti-tumor activity, and whether this activity affects key malignant phenotypes, including proliferation, clonogenic growth, cell death, migration, and invasion.

Therefore, defining the active fraction is an important first step in clarifying the anti-NSCLC potential of this plant and for guiding subsequent mechanistic and chemical studies. In the present study, phenotypic screening of natural herbal extracts was performed, identifying *Disporum cantoniense* extract (DE) as a candidate with inhibitory activity against NSCLC cells. Through solvent fractionation and bioactivity-guided evaluation, the petroleum ether fraction of *Disporum cantoniense* (DPF) was further identified as the principal active fraction. This fractionation strategy enables the enrichment of lipophilic bioactive compounds, which are often associated with enhanced cellular permeability and biological activity (26). The effects of DPF on NSCLC cell viability, proliferation, colony formation, cell death, migration, and invasion were then systematically examined, together with chemical profiling and mechanistic validation. Thus, the present study provides a pharmacological basis for further identifying the bioactive constituents of *Disporum cantoniense* and supports its potential value as a source of anti-NSCLC agents.

Materials and methods

Chemicals and reagents. Disporum cantoniense was purchased from the Chengdu Hehuachi Medicinal Materials Professional Market. Hoechst 33342 (cat. no. B2261) and propidium iodide (PI; cat. no. P4170) were purchased from Merck KGaA. In addition, 3-methyladenine (3-MA; cat. no. S2767) was purchased from Selleck Chemicals. Rapamycin (Rap; cat. no. T1537), compound C (CC; cat. no. T6146), gefitinib (Gefi; cat. no. T1181), ULK101 (cat. no. T5403), Z-VAD-FMK (ZVF; cat. no. T7020) and SCH772984 (SCH; cat. no. T6066) were obtained from TargetMol Chemicals Inc. Crystal violet staining solution (cat. no. C0121) and GreenNuc™ Live Cell Caspase-3 Activity Detection Kit (cat. no. C1168M) were

obtained from Beyotime Biotechnology. The Lipomaster 3000 Transfection Reagent (cat. no. TL301-02) was obtained from Vazyme Biotech Co., Ltd. The Annexin V-FITC/PI apoptosis detection kit (cat. no. FXP018) was purchased from Beijing 4A Biotech Co., Ltd. Plasmids, including enhanced green fluorescent protein EGFP-LC3 (cat. no. 11546) and ptfLC3 (cat. no. 21074) were obtained from Addgene, Inc. The primary antibodies used in the present study, including phosphorylated (p)-AMPK (cat. no. 2535), mTOR (cat. no. 2983S), p-ULK1 (Ser555; unc-51 like autophagy activating kinase 1; cat. no. 5869), p-ULK1 (Ser757; cat. no. 6888), p-MEK (cat. no. 9154S), MEK (cat. no. 4694S) and ERK (cat. no. 4695S), were purchased from Cell Signaling Technology, Inc. Antibodies from Proteintech Group, Inc. included GAPDH (cat. no. 60004-1-lg), LC3 (cat. no. 14600-1-AP), ULK1 (cat. no. 29005-2-AP), AMPK (cat. no. 10929-2-AP), p-mTOR (cat. no. 67778-1-lg), Bax (cat. no. 50599-2-lg) and Bcl-2 (cat. no. 68103-1-lg). p-ERK (cat. no. HY-P80814) was obtained from MedChemExpress. The cleaved caspase-3 antibody (cat. no. P20025) was obtained from Promab Biotechnologies, Inc. All reagents and antibodies were obtained from commercial sources and their specificity was validated by the respective manufacturers.

Plant material preparation and extraction. Roots and rhizomes of *Disporum cantoniense* were purchased, authenticated and processed for extraction. Dried plant material was extracted using 75% ethanol under controlled conditions to obtain crude DE. The extract was concentrated under reduced pressure, lyophilized and stored at -20˚C until use. The stock solution of DE was prepared by dissolving the lyophilized extract in DMSO and diluting to the desired concentrations with culture medium immediately before use, with the final DMSO concentration kept below 0.1% (v/v) (27).

Fractionation of the crude extract. Crude DE was subjected to sequential solvent partitioning to yield four fractions of differing polarity: DPF, ethyl acetate fraction (DEF), n-butanol fraction (DNF) and aqueous fraction (DWF). Briefly, the crude extract was suspended in water and partitioned successively with petroleum ether, ethyl acetate and n-butanol. Each organic layer was collected, evaporated to dryness under reduced pressure, before being stored at -20˚C. The fractions were reconstituted in DMSO for biological evaluation (28).

Chemical profiling by ultra-high-performance liquid chromatography quadrupole time-of-flight-tandem mass spectrometry (UHPLC-Q/TOF-MS/MS). Chemical composition of the DPF fraction was characterized using UHPLC-Q/TOF-MS/MS (29). The DPF fraction was dissolved and filtered through a 0.22-μm polytetrafluoroethylene membrane prior to injection. Chromatographic separation was performed on a C_{18} column with a gradient elution program using water and acetonitrile (both containing 0.1% formic acid) as mobile phases. Mass spectrometric detection was performed in both positive and negative ionization modes, with data acquired over a mass-to-charge ratio (m/z) range of 100-1,000. The total ion chromatogram and diode-array detector chromatogram recorded at 210 nm were obtained. Compound identification was performed by comparing molecular formulae and MS/MS fragmentation patterns with reference data available in databases such as the Human Metabolome Database (https://hmdb.ca/), Dictionary of Natural Products (http://dnp.chemnetbase.com/) and METLIN (https://metlin.scripps.edu/). A total of 14 small-molecule constituents were annotated.

Cell culture. A549 cells (cat. no. CCL-185; American Type Culture Collection), a human NSCLC cell line, and H1299 cells (cat. no. CRL-5803; American Type Culture Collection), a human lung adenocarcinoma cell line, were cultured in RPMI-1640 medium supplemented with 10% FBS and 1% penicillin-streptomycin. BEAS-2B cells (cat. no. CRL-9609; American Type Culture Collection), a normal human bronchial epithelial cell line, were cultured in DMEM/F-12 medium supplemented with 10% FBS, 100 U ml^{-1} penicillin, and 100 μg ml^{-1} streptomycin. Immortalized wild-type (WT) and Bax-Bak double knockout (DKO) mouse embryonic fibroblast (MEF) cells were provided by Professor Shigeomi Shimizu (Tokyo Medical and Dental University, Medical Research Institute, Tokyo, Japan). Immortalized $Atg7^{+/+}$ and $Atg7^{-/-}$ MEFs were provided by Professor Masaaki Komatsu (Juntendo University, School of Medicine, Tokyo, Japan). These cells were cultured in complete DMEM medium. All cells were maintained at 37˚C in a humidified atmosphere containing 5% CO_2 (30).

Natural product screening and cell viability assays. For initial screening, A549 and BEAS-2B cells were seeded in multi-well plates and treated with a panel of crude herbal extracts at fixed concentrations for a defined period. Cell viability was determined using an MTT assay. In brief, cells were seeded in 96-well plates at $5x10^3$ cells per well, allowed to adhere overnight, and subsequently treated with the indicated drugs at 31.3, 62.5, 125 or 250 μg/ml, or with the control (Ctrl), for 24 h at 37˚C. Following treatment, the purple formazan crystals were dissolved in DMSO, and the absorbance was measured at 490 nm using a microplate reader, and cell viability was calculated relative to untreated control cells. The resulting data were used to generate heatmaps, bar charts, and dose-response curves. All viability experiments were performed in at least three independent replicates (31).

Real-time cell analysis. Real-time monitoring of cell proliferation was performed using the Agilent xCELLigence Real-Time Cell Analysis system (Agilent Technologies) (32). A549 and H1299 cells were each seeded in E-plates at a density of $5x10^3$ cells/well. After cells had adhered and entered log-phase growth (24 h), DPF was added at 25, 50, 100 and 200 μg/ml. The cell index, which reflects cell number, morphology, and adhesion, was recorded every 15 min over a 25-h monitoring period. Data were normalized to the time point of drug addition for comparison across treatment groups.

Transwell invasion assay. Cell invasion was assessed using 24-well Transwell chambers with 8-μm-pore polycarbonate membranes pre-coated with Matrigel (Corning, Inc.) at 37˚C for 2 h. A549 and H1299 cells were serum-starved overnight and then seeded at $5x10^4$ cells in serum-free medium containing DPF at 25, 50, 100 and 200 μg/ml in the upper chamber. The lower chamber was filled with medium containing 10% FBS as a chemoattractant. After 24 h of incubation at 37˚C,

non-invading cells on the upper surface were removed with cotton swabs. Cells that had migrated to the lower surface were fixed with 4% paraformaldehyde for 15 min at room temperature (20-25˚C), stained with 0.1% crystal violet for 20 min at room temperature, and imaged under a light microscope (magnification, x10). Invaded cells were quantified by counting in five randomly selected fields per membrane (33).

Hoechst 33342/PI dual staining. Cell death was evaluated using Hoechst 33342/PI dual staining (34). A549 and H1299 cells were seeded in multi-well plates and treated with drugs at 50, 100 and 200 μg/ml for 24 h at 37˚C. Following treatment, cells were incubated with Hoechst 33342 (10 μg/ml) and PI (5 μg/ml) for 15-20 min at 37˚C in the dark. Fluorescence images were captured using an inverted fluorescence microscope (magnification: x10; scale bar: 200 μm). The cell death rate was quantified as the ratio of PI-positive cells to total Hoechst-stained cells in at least five randomly selected fields per condition.

Lactate dehydrogenase (LDH) release assay. Membrane-damaging cytotoxicity was assessed using an LDH release assay. A549 and H1299 cells were seeded in 96-well plates and treated with DPF at 25, 50, 100 and 200 μg/ml for 24 h at 37˚C. After treatment, the culture supernatants were collected, and LDH activity was measured according to the manufacturer's instructions using a commercial LDH Cytotoxicity Assay Kit (cat. no. BL1405A; Biosharp Life Sciences). The absorbance was measured using a microplate reader, and LDH release (%) was calculated according to the manufacturer's instructions using the following formula: (Experimental LDH release-spontaneous LDH release)/(maximum LDH release-spontaneous LDH release) x100.

Colony formation assay. Long-term proliferative and clonogenic capacity was assessed by colony formation assay. A549 and H1299 cells were seeded at $0.8x10^3$ cells per well in 6-well plates and allowed to attach for 24 h. Cells were then treated with DPF at 25, 50, 100 and 200 μg/ml, or with Gefi as a positive control, at 37˚C. After 12 days of culture, during which the medium was replenished every 3 days, colonies were fixed with 4% paraformaldehyde for 15 min at room temperature, stained with 0.1% crystal violet for 20 min at room temperature, and images were captured. Colonies consisting of ≥50 cells were counted manually using ImageJ software (version 1.53k; National Institutes of Health), and representative images were acquired (35).

Wound healing assay. Cell migration was evaluated using the wound-healing assay (36). A549 and H1299 cells were seeded in 6-well plates and cultured until reaching ~90% confluence. Cells were serum-starved in serum-free medium overnight. A linear scratch was made across each monolayer using a sterile 200-μl pipette tip. Detached cells were removed by washing with PBS and fresh serum-reduced medium containing 1% FBS and DPF at concentrations of 25, 50, 100, and 200 μg/ml was added. Images of the wound area were captured at 0 and 24 h using a phase-contrast microscope. The remaining wound area was quantified using ImageJ software (version 1.53k; National Institutes of Health) and expressed as the percentage of the initial wound area at 24 h. A higher remaining wound area indicated reduced migratory capacity.

Transcriptomic profiling and bioinformatic analysis. Total RNA was extracted from A549 cells treated with DPF or Ctrl using TRIzol reagent (Invitrogen; Thermo Fisher Scientific, Inc.) according to the manufacturer's protocol. RNA integrity was verified using an Agilent 2100 Bioanalyzer (Agilent Technologies) and samples with an RNA integrity number ≥7.0 were used for library construction. Sequencing libraries were prepared using a NEBNext Ultra II Directional RNA Library Prep Kit for Illumina (cat. no. E7760S; New England Biolabs, Inc.). The concentration of the final library was measured using a Qubit 4.0 Fluorometer (Thermo Fisher Scientific, Inc.) and adjusted to a final loading concentration of 2 nM prior to loading. Sequencing was performed on an Illumina NovaSeq 6000 platform to generate 150-bp paired-end reads. Raw sequencing reads were quality-filtered and aligned to the human reference genome (GRCh38) using HISAT2 (v2.2.1; https://ccb.jhu.edu/software/hisat2/index.shtml). Gene expression was quantified using featureCounts (Subread v2.0.1) and differential expression analysis was performed using DESeq2 (v1.38.0; https://bioconductor.org/packages/DESeq2), with genes considered differentially expressed at adjusted $P<0.05$. Principal component analysis (PCA) was performed to assess overall transcriptomic variation between groups.

Differentially expressed genes (DEGs) were visualized using volcano plots and heatmaps generated with R packages 'ggplot2' (v3.4.0) and 'pheatmap' (v1.0.12) using R software (version 4.2.2). Gene Ontology (GO) enrichment analysis and Kyoto Encyclopedia of Genes and Genomes (KEGG) pathway enrichment analysis were carried out using clusterProfiler (v4.6.0; http://bioconductor.org/packages/clusterProfiler) to identify significantly enriched biological processes and signaling pathways among the DEGs (37).

Network pharmacology analysis. To complement the transcriptomic findings, a network pharmacology approach was employed. The putative molecular targets of the 14 annotated chemical constituents of DPF were predicted using publicly available databases, including SwissTargetPrediction (http://www.swisstargetprediction.ch/), PharmMapper (http://www.lilab-ecust.cn/pharmmapper/) and Similarity Ensemble Approach (http://sea.bkslab.org/). Disease-associated targets for NSCLC were retrieved from databases including GeneCards (https://www.genecards.org/), Online Mendelian Inheritance in Man (OMIM; https://www.omim.org/), and DisGeNET (https://www.disgenet.org/). Overlapping targets between compound-predicted targets and disease targets were identified and subjected to GO and KEGG pathway enrichment analyses to determine enriched biological processes and signaling pathways. The results were compared with the transcriptomic findings to identify converging pathways (38).

Western blotting analysis. A549 and H1299 cells were lysed in RIPA buffer (Beyotime Biotechnology) supplemented with protease and phosphatase inhibitor cocktails. Protein concentrations were determined by a BCA assay. Equal amounts of total protein (40 μg per lane) were separated on 12% gels using

SDS-PAGE and transferred to PVDF membranes. Membranes were blocked with 5% non-fat milk or 5% bovine serum albumin (BSA; MilliporeSigma) in TBST (TBS containing 0.1% Tween-20) for 1 h at room temperature. The membranes were then incubated overnight at 4˚C with the indicated primary antibodies (diluted at 1:10,000 for anti-GAPDH and 1:1,000 for all others). After washing, the membranes were incubated with secondary antibodies, including HRP-conjugated goat anti-rabbit IgG (diluted 1:2,000) or HRP-conjugated goat anti-mouse IgG (diluted 1:2,000), for 1 h at room temperature. Protein bands were detected using ECL reagent, and band intensities were quantified using ImageJ software (National Institutes of Health). Protein expression levels were normalized to GAPDH or total protein as appropriate, and phosphorylation levels were expressed as the ratio of phosphorylated to total protein (39).

GFP-LC3 puncta formation assay. A549 and H1299 cells were transiently transfected with an EGFP-LC3 plasmid (GFP-LC3; Addgene, cat. no. 11546) (2 μg/ml) using Lipomaster 3000 (TL301; Vazyme Biotech Co., Ltd.) according to the manufacturer's instructions. At 24 h post-transfection, cells were treated with DPF at 50, 100 and 200 μg/ml at 37˚C, with Rap as a positive control, for a further 24 h. Where indicated, cells were co-treated with pharmacological inhibitors, including CC (AMPK inhibitor), ULK101 (ULK1 inhibitor), or SCH (ERK inhibitor) at 37˚C for 24 h. After treatment, the cells were fixed with 4% paraformaldehyde for 15 min at room temperature, counterstained with Hoechst 33342 for 10 min at room temperature in the dark for nuclear visualization, and imaged using a confocal laser scanning microscope at x63 magnification (scale bar, 20 μm). The number of GFP-LC3 puncta per cell was quantified in at least 30 cells per condition across three independent experiments (40).

The ptfLC3 autophagic flux assay. To distinguish between autophagosome formation and autolysosome maturation, A549 and H1299 cells were transfected with a tandem ptfLC3 reporter plasmid (2 μg/ml; cat no. 21074; Addgene, Inc.) using Lipomaster 3000 at 37˚C for 24 h. In this system, autophagosomes appear as yellow puncta (GFP^+/RFP^+), whereas autolysosomes, in which GFP fluorescence is quenched by the acidic pH, appear as red-only puncta (GFP^-/RFP^+). At 24 h post-transfection, cells were treated with DPF (100 μg/ml) or Rap (10 μM; positive control) at 37˚C for 24 h. The cells were then fixed with 4% paraformaldehyde for 15 min at room temperature, counterstained with Hoechst 33342 for 10 min at room temperature in the dark, and imaged by confocal microscopy at x63 magnification (scale bar, 20 μm). The fluorescence intensities of RFP and GFP were quantified and the RFP/GFP ratio was calculated to assess autophagic flux (41).

Flow cytometric analysis of apoptosis. Apoptosis was quantified by Annexin V-FITC/PI dual staining followed by flow cytometry. A549 and H1299 cells were treated with DPF at 50, 100 and 200 μg/ml for 24 h at 37˚C, collected by trypsinization, washed twice with cold PBS, and resuspended in 1x binding buffer. Cells were stained with Annexin V-FITC and PI for 15 min at room temperature in the dark according to the manufacturer's protocol. Stained cells were analyzed on a flow cytometer (BD FACSVerse; BD Biosciences). The proportion of early apoptotic (Annexin V^+/PI^-) and late apoptotic (Annexin V^+/PI^+) cells was determined using FlowJo software (version 10.8.1; BD Biosciences) and total apoptotic rates were calculated as the sum of early and late apoptotic populations (42).

Caspase-3 fluorescence staining. Caspase-3 activation was visualized using a fluorescent caspase-3 activity detection kit. Cells were seeded on coverslips and treated with DPF at 50, 100 and 200 μg/ml for 24 h at 37˚C. Where indicated, cells were co-treated with pharmacological inhibitors 3-MA, CC, ULK101 or SCH for 24 h at 37˚C. Cells were then stained with the caspase-3-specific fluorescent substrate according to the manufacturer's instructions. Nuclei were counterstained with Hoechst 33342 for 10 min at room temperature in the dark. Fluorescence images were acquired using an inverted fluorescence microscope (magnification: x10; scale bar: 200 μm). Caspase-3 fluorescence intensity was quantified using ImageJ software (National Institutes of Health) and expressed as a percentage relative to the control group (43).

Molecular docking. Molecular docking simulations were performed to assess the potential binding interactions between BBG-D, a chemical constituent identified in the DPF fraction, and the catalytic domains of AMPK and MEK (44). The three-dimensional structures of the target proteins were retrieved from the Protein Data Bank (https://www.rcsb.org/) and prepared using standard protocols (38), including removal of water molecules and co-crystallized ligands, addition of hydrogen atoms, and energy minimization. The three-dimensional structure of BBG-D was generated and energy-minimized using Chem3D software (version 20.0; PerkinElmer, Inc.). Docking simulations were carried out using AutoDock Vina (version 1.2.5; https://vina.scripps.edu/). The binding poses with the most favorable binding energies were selected, and key protein-ligand interactions (hydrogen bonds, hydrophobic contacts, and π-π stacking) were visualized and analyzed using PyMOL (version 2.5.0; Schrödinger, LLC; https://www.pymol.org/).

In vivo xenograft tumor model. All animal experiments were approved by the Institutional Animal Care and Use Committee of Southwest Medical University (Luzhou, China; approval no. 20240514-004) and were performed in accordance with the institutional guidelines for animal care and use (45). A total of 24 male BALB/c nude mice (age, 5-6 weeks; weight, 18-22 g; GemPharmatech Co. Ltd.) were used in the present study. Mice were maintained under specific-pathogen-free conditions at 22±2˚C and 50±10% humidity under a 12 h light/dark cycle, with free access to sterilized water and standard rodent chow. To establish the subcutaneous xenograft tumor model, A549 cells were harvested during the logarithmic growth phase and resuspended in a 1:1 mixture of serum-free medium and Matrigel. A total of $5x10^6$ A549 cells in 100 μl suspension were subcutaneously injected into the right flank of each mouse. When the mean tumor volume reached ~100 mm^3, the mice were randomly divided into four groups (n=6 per group): i) Vehicle control; ii) Gefi (20 mg/kg); iii) DPF low-dose group (40 mg/kg); and iv) DPF high-dose group (80 mg/kg). Blinding

was not performed during drug administration; however, tumor size and body weight were assessed by an investigator blinded to the treatment allocation. Tumor size was measured using digital calipers by the same operator to minimize inter-observer variability, and body weight was measured at a fixed time of day using a calibrated electronic scale throughout the experiment. DPF and Gefi were prepared in a vehicle composed of double-distilled water, polyethylene glycol 400, and DMSO at a volume ratio of 5:4:0.5 (v/v/v) and were administered by intraperitoneal injection once daily for 15 days. The vehicle control group received the same volume of vehicle via intraperitoneal injection. Tumor length and width were measured every 2 days using digital calipers, and tumor volume was calculated according to the formula: $V=0.5 \times \text{length} \times \text{width}^2$. Body weight was recorded throughout the treatment period.

The humane endpoints were defined as a tumor volume >1,500 mm^3, severe ulceration or necrosis of the tumor, body weight loss >20%, marked lethargy, impaired mobility, or other signs of severe distress. During the experiment, no mouse reached the predefined tumor-volume endpoint. The maximum observed tumor dimensions were 16.91x12.96 mm, corresponding to a maximum calculated tumor volume of 1,420 mm^3. At the end of the experiment, mice were anesthetized through intraperitoneal administration of pentobarbital sodium at 150 mg/kg and then euthanized by cervical dislocation. Mortality was determined by the absence of respiration, heartbeat, corneal reflex, and response to toe pinch. Tumors were excised, photographed, and weighed. Major organs, including the heart, liver, spleen, lung, and kidney, were collected and weighed to evaluate gross systemic toxicity. Tumor tissues were processed for histopathological, TUNEL, and immunohistochemical analyses (45).

Histopathology, TUNEL staining and immunohistochemistry. Excised tumor tissues were fixed in 4% paraformaldehyde at 4˚C for 24 h, embedded in paraffin, and sectioned at 4-5 μm thickness. For histopathological evaluation, sections were stained with hematoxylin for 5 min and counterstained with eosin for 2 min at room temperature. The H&E-stained sections were then examined under a light microscope to assess tumor morphology and tissue integrity (27,46). Apoptosis in tumor tissues was detected using a TUNEL assay with the In Situ Cell Death Detection Kit (cat. no. 11684795910; Roche Diagnostics) according to the manufacturer's instructions. Sections were mounted with VECTASHIELD® Antifade Mounting Medium (Vector Laboratories, Inc.), and TUNEL-positive cells were visualized under a fluorescence microscope at x10 magnification (scale bar, 200 μm). Green fluorescent TUNEL-positive cells were quantified in five randomly selected fields of view per section (47). For immunohistochemical staining, deparaffinized and rehydrated sections were subjected to heat-mediated antigen retrieval in citrate buffer (pH 6.0) at 95-100˚C for 15 min. Endogenous peroxidase activity was quenched with 3% hydrogen peroxide. Sections were blocked with 10% normal goat serum (Solarbio Science & Technology Co., Ltd.) for 30 min at room temperature and then incubated overnight at 4˚C with primary antibodies against Bax (1:200), mTOR (1:200), ERK (1:200) and LC3 (1:200). After washing, the sections were incubated with biotinylated goat anti-rabbit IgG or goat anti-mouse IgG secondary antibody (1:500) for 1 h at room temperature, followed by incubation with streptavidin-HRP conjugate for 30 min at room temperature. Staining was developed using DAB, and sections were counterstained with hematoxylin, dehydrated, and mounted. Images were captured at x10 magnification (scale bar, 200 μm), and the staining intensity was quantified using ImageJ software (version 1.53k; National Institutes of Health) (48).

Statistical analysis. All data are presented as the mean ± SD from at least three independent experiments unless otherwise stated. Statistical comparisons among multiple groups were performed using one-way ANOVA followed by Tukey's or Dunnett's post hoc test. For tumor growth curves, two-way repeated-measures ANOVA followed by Sidak's post hoc test was used. Statistical analyses were conducted using GraphPad Prism (version 9.0; Dotmatics). $P<0.05$ was considered to indicate a statistically significant difference.

Results

Natural extract screening identifies Disporum cantoniense that selectively inhibits NSCLC cells. To identify natural products with selective anti-tumor activity, a panel of herbal extracts was screened in A549 and BEAS-2B cells. Heatmap analysis shows that while the majority of extracts produced minimal changes in cell viability, one extract markedly decreased viability in A549 cells but had a weaker effect on BEAS-2B cells (Fig. 1A and B). These observations suggest that this extract selectively reduces NSCLC cell viability. This extract, identified as DE, was subsequently examined in dose-response assays. DE caused a concentration-dependent decrease in A549 cell viability, with statistically significant inhibition observed at 125 and 250 μg/ml ($P<0.001$) (Fig. 1C). By contrast, BEAS-2B cells exhibited no significant reduction in cell viability across the same concentration range (Fig. 1D). Thus, DE may exhibit preferential cytotoxicity toward NSCLC cells over normal lung epithelial cells. To identify the bioactive component responsible for this activity, DE was fractionated into DPF, DEF, DNF, and DWF. Among these fractions, DPF produced the most pronounced reduction in A549 cell viability. Compared with BEAS-2B cells, A549 cells exhibited significantly lower viability following treatment with DPF at 50 μg/ml ($P<0.01$), 100 μg/ml ($P<0.001$) and 200 μg/ml ($P<0.01$), whereas BEAS-2B cells showed relatively modest changes in viability (Fig. 1E-H), indicating that DPF represents the primary active fraction within the DE. The inhibitory activity of DPF was further validated in H1299 cells. DPF treatment significantly decreased H1299 cell viability in a concentration-dependent manner, consistent with its activity in A549 cells (Fig. 1I). Chemical profiling of the DPF fraction using UHPLC-Q/TOF-MS/MS revealed a number of distinct chromatographic peaks, with 14 small-molecule constituents being annotated (Fig. 1J; Table I). These findings provide a basis for subsequent chemical and mechanistic studies. Overall, the screening identified *Disporum cantoniense*, particularly its DPF fraction, as a selective inhibitor of NSCLC cell viability.

DPF inhibits proliferation, invasion, clonogenicity and migration and further induces membrane-damaging cytotoxicity in NSCLC cells. To evaluate the cellular effects of

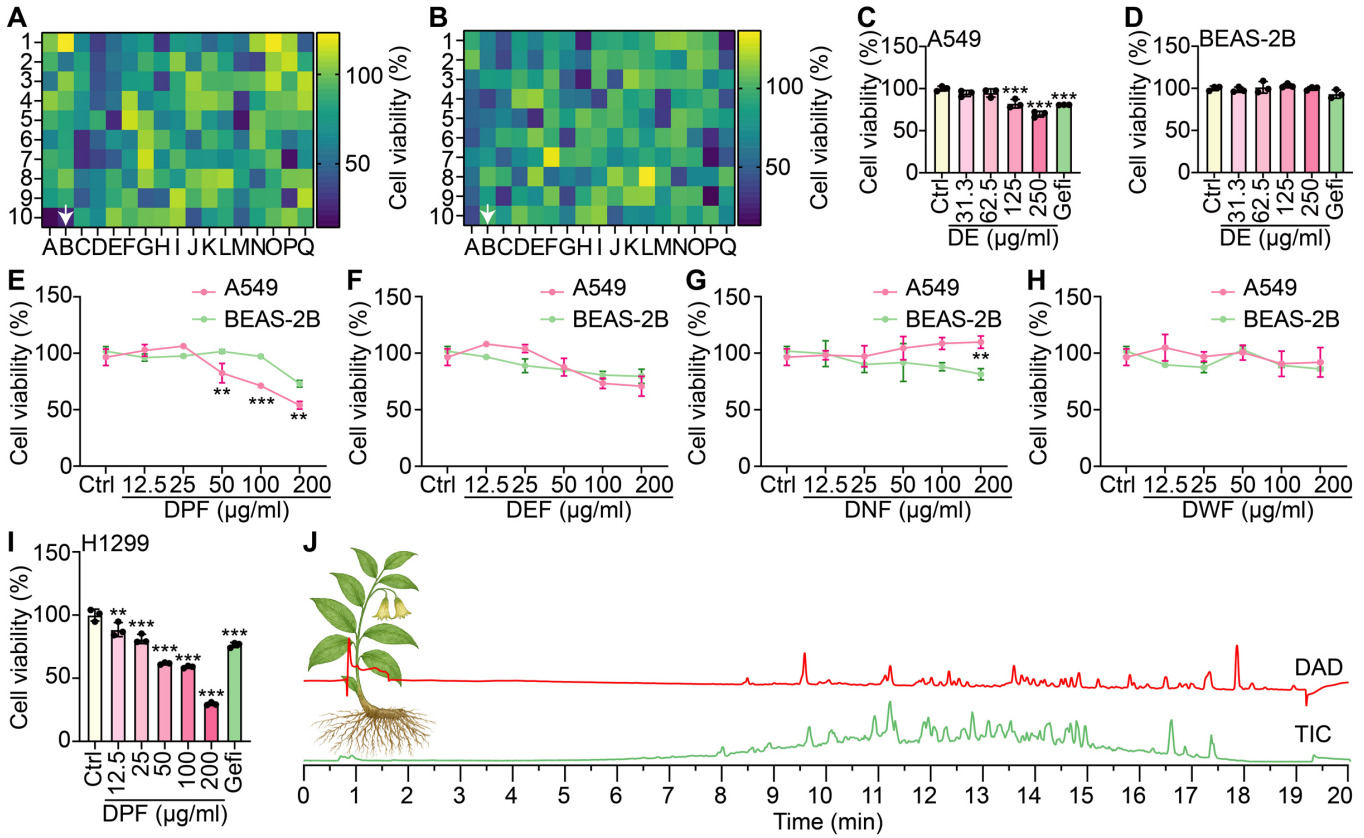


Figure 1. Cytotoxicity screening in A549 cells and chemical profiling of *Disporum cantoniense*. (A and B) Heatmaps showing cell viability in (A) A549 and (B) BEAS-2B cells treated with crude herbal extracts. The white arrows indicate DE. (C and D) Quantification of cell viability in (C) A549 and (D) BEAS-2B cells treated with different concentrations of DE. (E-H) Line graphs showing the viability of A549 and BEAS-2B cells treated with four fractions of DE, including (E) DPF, (F) DEF, (G) DNF and (H) DWF, at the indicated concentrations. (I) Cell viability of H1299 cells treated with various concentrations of DPF. (J) Representative image of *Disporum cantoniense* and ultra-high-performance liquid chromatography quadrupole time-of-flight tandem mass spectrometry chromatograms of DPF displaying the TIC and the corresponding DAD chromatogram recorded at 210 nm. Statistical significance is denoted as **P<0.01 and ***P<0.001. Data are presented as the mean ± SD of three independent experiments. DE, *Disporum cantoniense* extract; DEF, *Disporum cantoniense* ethyl acetate fraction; DNF, *Disporum cantoniense* n-butanol fraction; DPF, *Disporum cantoniense* petroleum ether fraction; DWF, *Disporum cantoniense* aqueous fraction; TIC, total ion chromatogram; DAD, diode-array detector; Ctrl, vehicle; Gefi, gefitinib.

the active fraction DPF, real-time proliferation dynamics were first monitored in A549 and H1299 cells. Real-time cell analysis showed that DPF markedly suppressed the proliferation-associated cell index in both cell lines in a concentration-dependent manner, with higher doses producing rapid and sustained reductions during the monitoring period (Fig. 2A and B). These findings indicate that DPF effectively reduces NSCLC cell proliferation.

The impact of DPF on invasive behavior was assessed using Transwell assays. DPF decreased the number of invading A549 cells in a concentration-dependent manner, with significant reductions observed at 25 μg/ml (P<0.05), 50 μg/ml (P<0.01), and 100 and 200 μg/ml (P<0.001). In H1299 cells, significant reductions were observed at all tested concentrations from 25 to 200 μg/ml (P<0.001) (Fig. 2C-E). Hoechst/PI staining further showed that DPF increased PI-positive cell death in A549 cells at 50 μg/ml (P<0.01) and at 100 and 200 μg/ml (P<0.001). In H1299 cells, PI-positive cell death was significantly increased at all tested concentrations from 50 to 200 μg/ml (P<0.001) (Fig. 2F-H). To further determine whether DPF-induced viability loss was accompanied by membrane-damaging cytotoxicity, LDH release assays were performed. DPF treatment significantly increased LDH release in both A549 and H1299 cells in a concentration-dependent manner (Fig. 2I and J), indicating that DPF-induced cytotoxicity is associated with impaired membrane integrity. Long-term proliferative ability was examined using colony formation assays. DPF markedly reduced the number and size of colonies formed by A549 and H1299 cells, with progressively fewer colonies observed as DPF concentration increased (Fig. 2K and L). The impact of DPF on cell migration was then evaluated using wound-healing assays, which showed significantly suppressed wound closure after 24 h in A549 cells at all tested concentrations (25-200 μg/ml; P<0.001). In H1299 cells, significant inhibition of wound closure was also observed across the tested concentration range, with significance levels of P<0.01 or P<0.001 depending on the DPF concentration, resulting in a concentration-dependent reduction in migratory capacity (Fig. 2M-P). Collectively, these results suggest that DPF suppresses NSCLC cell proliferation, invasion, clonogenicity and migration, while also inducing membrane-damaging cytotoxicity.

DPF alters gene expression and modulates key pathways in A549 cells. To investigate the molecular effects of DPF treatment, transcriptomic profiling of A549 cells followed

Table I. Components identified in *Disporum cantoniense* petroleum ether fraction using ultra-high-performance liquid chromatography quadrupole time-of-flight tandem mass spectrometry.

No.	Retention time, min	Chemical name	Chemical formula	Molecular weight	$(M-H)^-$
1	7.160	Raspberry ketone	$C_{10}H_{12}O_2$	164.20	163.0765
2	8.254	Methyl cinnamate	$C_{10}H_{10}O_2$	162.19	161.0608
3	8.420	Syringaldehyde	$C_9H_{10}O_4$	182.17	181.0506
4	8.483	2'-β-D-glucopyranosyloxybenzyl-6-α-L-(4'-O-acetyl)-rhamnopyranosyloxy-2-hydroxy-3-methoxybenzoate	$C_{29}H_{36}O_{16}$	640.59	639.1931
5	9.567	(2S)-2,3-dihydroxypropyl-1,6,8-tridihydroxy-3-methyl-9,10-dioxoanthracene-2-carboxylate	$C_{19}H_{16}O_9$	388.32	387.0722
6	10.096	Neoechinulin A	$C_{19}H_{21}N_{3O2}$	323.39	322.1561
7	10.698	3-Hydroxy-1-(4-hydroxy-3,5-dimethoxyphenyl)-1-propanone	$C_{11}H_{14}O_5$	226.22	225.0768
8	10.912	Mycophenolic acid	$C_{17}H_{20}O_6$	320.33	319.1187
9	11.138	2-Hydroxybenzyl alcohol	$C_7H_8O_2$	124.13	123.0461
10	11.301	Glansreginic acid	$C_{12}H_{18}O_5$	242.27	241.1081
11	12.288	Nodakenetin	$C_{14}H_{14}O_4$	246.26	245.0819
12	13.060	Neoglabrazoide	$C_{21}H_{22}O_9$	418.39	417.1191
13	14.146	Icariol A2	$C_{22}H_{28}O_9$	436.45	435.1661
14	16.673	Mangiferin	$C_{22}H_{22}O_9$	430.40	429.1191

by differential gene expression analysis was performed. PCA revealed a clear separation between the DPF-treated group and the Ctrl group, with the first two principal components (PC1 and PC2) accounting for 68.34 and 18.17% of the total variance, respectively (Fig. 3A). This indicates that DPF treatment induced marked transcriptional changes in A549 cells. The volcano plot shows that 971 genes were upregulated and 767 genes were downregulated in the DPF-treated group compared with the Ctrl group, using an adjusted $P<0.05$ threshold (Fig. 3B).

These DEGs were further visualized through a heatmap (Fig. 3C), which demonstrated distinct gene expression profiles between the two groups. In the heatmap, red and blue represent upregulated and downregulated genes, respectively, in DPF-treated A549 cells. GO enrichment analysis based on the transcriptomic DEGs revealed significant enrichment in biological processes associated with the 'apoptotic signaling pathway', 'negative regulation of cell migration' and 'regulation of cell growth' (Fig. 3D). KEGG pathway analysis of the DEGs further identified significant enrichment in pathways associated with cell signaling, metabolism and disease progression, including the 'MAPK signaling pathway', 'mTOR signaling pathway' and other cancer-associated pathways (Fig. 3E and F). Notably, network pharmacology analysis was largely consistent with the transcriptomic findings. KEGG analysis revealed significant enrichment in 'non-small cell lung cancer', 'AMPK signaling pathway', 'mTOR signaling pathway', 'autophagy-animal', 'mitophagy-animal', 'MAPK signaling pathway' and further apoptosis-associated pathways (Fig. S1). In addition, GO analysis highlighted biological processes such as 'positive regulation of autophagy', 'positive regulation of apoptotic signaling pathway', 'positive regulation of MAPK cascade' and 'positive regulation of ERK1 and ERK2 cascade' (Fig. S2). Collectively, these results support that DPF suppresses NSCLC through coordinated regulation of autophagy- and apoptosis-associated signaling and may involve the AMPK/mTOR pathway network.

DPF activates autophagy in NSCLC cells through AMPK/mTOR/ULK1 and MEK/ERK pathways. Based on the transcriptomic and network pharmacology analyses, which suggested the involvement of autophagy-associated signaling pathways, the present study next investigated whether DPF induces autophagy in NSCLC cells and explored the underlying molecular mechanisms. Autophagy induction and flux were evaluated by measuring LC3 conversion, GFP-LC3 puncta formation, and tandem mRFP-GFP-LC3 reporter signals in A549 and H1299 cells. DPF treatment increased LC3-II levels and the LC3-II/LC3-I ratio in a concentration-dependent manner in both A549 and H1299 cells. At 200 μg/ml, both LC3-II levels and the LC3-II/LC3-I ratio were significantly increased in A549 cells ($P<0.05$) and H1299 cells ($P<0.05$) (Fig. 4A-D), indicating enhanced autophagosome formation. Consistently, fluorescence microscopy showed that DPF significantly increased the number of GFP-LC3 puncta in both cell lines in a concentration-dependent manner (Fig. 4E, G, I and J).

To further determine whether DPF promoted autophagic flux rather than causing autophagosome accumulation, a tandem mRFP-GFP-LC3 reporter assay was employed. DPF treatment significantly increased RFP fluorescence intensity and elevated the RFP/GFP ratio in both A549 and H1299 cells (Fig. 4F, H, K and L), indicating that DPF enhances autophagic

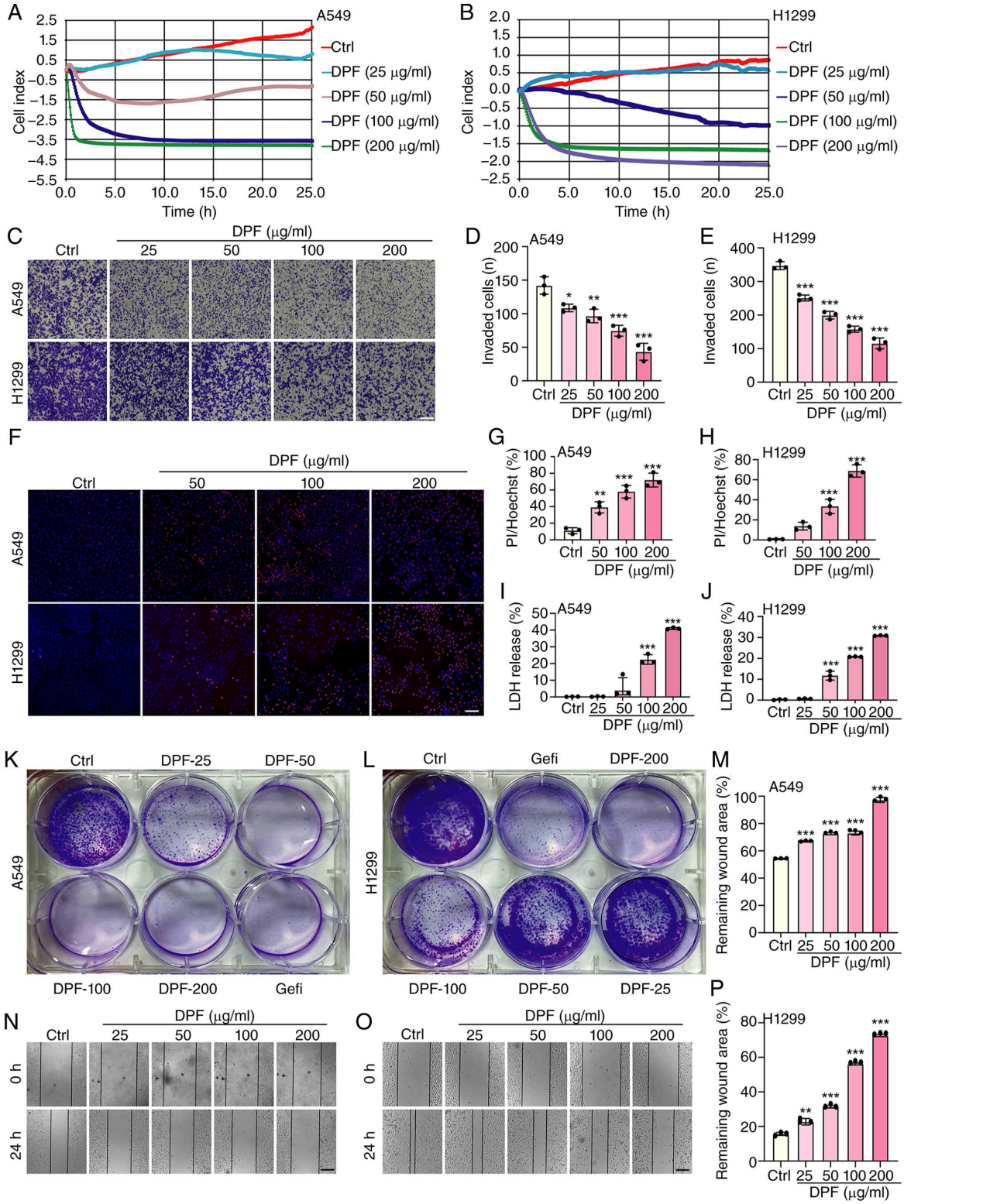


Figure 2. DPF inhibits proliferation, invasion, colony formation and migration and induces membrane-damaging cytotoxicity in NSCLC cells. (A and B) Real-time cell analysis curves showing the cell index of (A) A549 and (B) H1299 cells treated with DPF at the indicated concentrations over 25 h. (C) Representative images of Transwell invasion assays in A549 and H1299 cells following treatment with different concentrations of DPF (magnification, x10; scale bar, 200 μm). (D and E) Quantification of invaded (D) A549 and (E) H1299 cells after DPF treatment. (F) Representative fluorescence images of Hoechst/PI staining in A549 and H1299 cells treated with increasing concentrations of DPF. Nuclei were stained with Hoechst and PI-positive cells indicate membrane-compromised dead cells (scale bar, 200 μm). (G and H) Quantification of PI-positive cell death in (G) A549 and (H) H1299 cells after DPF treatment, expressed as the percentage of PI-positive cells relative to Hoechst-stained cells. (I and J) LDH release assay showing membrane-damaging cytotoxicity in (I) A549 and (J) H1299 cells following DPF treatment. (K and L) Representative colony formation images of (K) A549 and (L) H1299 cells treated with DPF at the indicated concentrations or Gefi. (M) Quantification of the remaining wound area in A549 cells following DPF exposure. (N and O) Representative wound-healing images showing the migration of (N) A549 and (O) H1299 cells at 0 and 24 h after DPF treatment (magnification, x10; scale bar, 200 μm). (P) Quantification of the remaining wound area in H1299 cells. Statistical significance is denoted as *P<0.05, **P<0.01 and ***P<0.001. Data are presented as the mean ± SD of three independent experiments. DPF, *Disporum cantoniense* petroleum ether fraction; NSCLC, non-small cell lung cancer; Gefi, gefitinib; Ctrl, vehicle; LDH, lactate dehydrogenase; PI, propidium iodide.

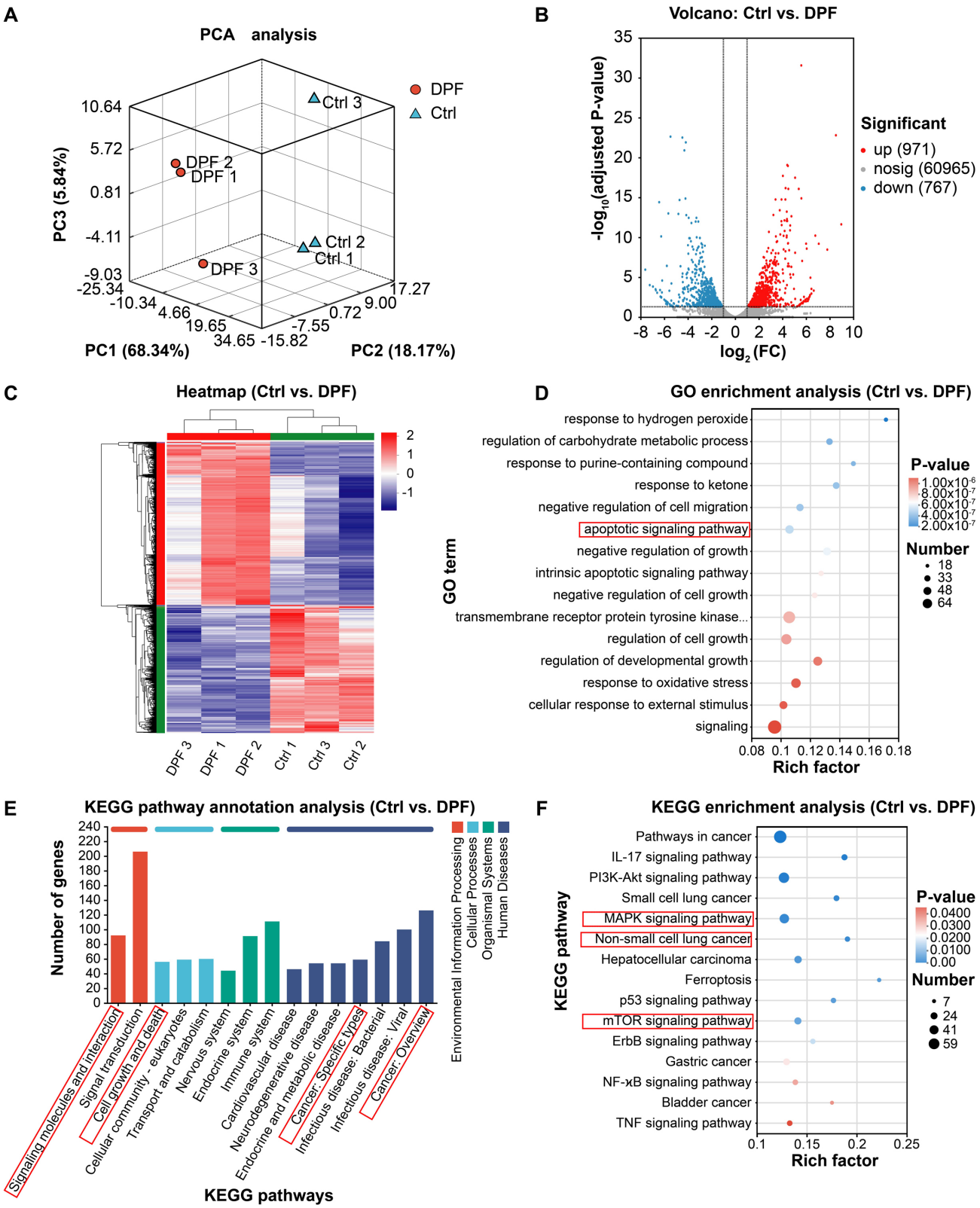


Figure 3. Transcriptomic profiling and pathway enrichment analysis of DPF-treated A549 cells. (A) PCA of transcriptomic data comparing Ctrl and DPF-treated A549 cells. PC1, PC2 and PC3 explain 68.34, 18.17 and 5.84% of the variance, respectively. (B) Volcano plot showing DEGs between Ctrl and DPF-treated A549 cells. Red points indicate significantly upregulated genes, while blue points indicate significantly downregulated genes, with 971 upregulated and 767 downregulated genes (adjusted P<0.05). (C) Heatmap illustrating the expression levels of DEGs between Ctrl and DPF-treated A549 cells. Genes are represented by rows and samples are represented by columns, with color intensity indicating gene expression levels. (D) GO enrichment analysis of DEGs comparing Ctrl and DPF-treated A549 cells. The analysis highlights significant biological processes, including 'apoptotic signaling pathway', 'negative regulation of cell migration' and 'negative regulation of growth'. (E) KEGG pathway enrichment analysis of DEGs between Ctrl and DPF-treated A549 cells. Pathways associated with cell signaling, metabolism and diseases are significantly enriched in the DPF-treated group. (F) KEGG pathway enrichment analysis highlighting the most enriched pathways in DPF-treated A549 cells. Notable pathways include the 'MAPK signaling pathway', the 'mTOR signaling pathway' and pathways in cancer. DPF, *Disporum cantoniense* petroleum ether fraction; PCA, principal component analysis; Ctrl, vehicle; DEGs, differentially expressed genes; GO, Gene Ontology; KEGG, Kyoto Encyclopedia of Genes and Genomes; FC, fold change.

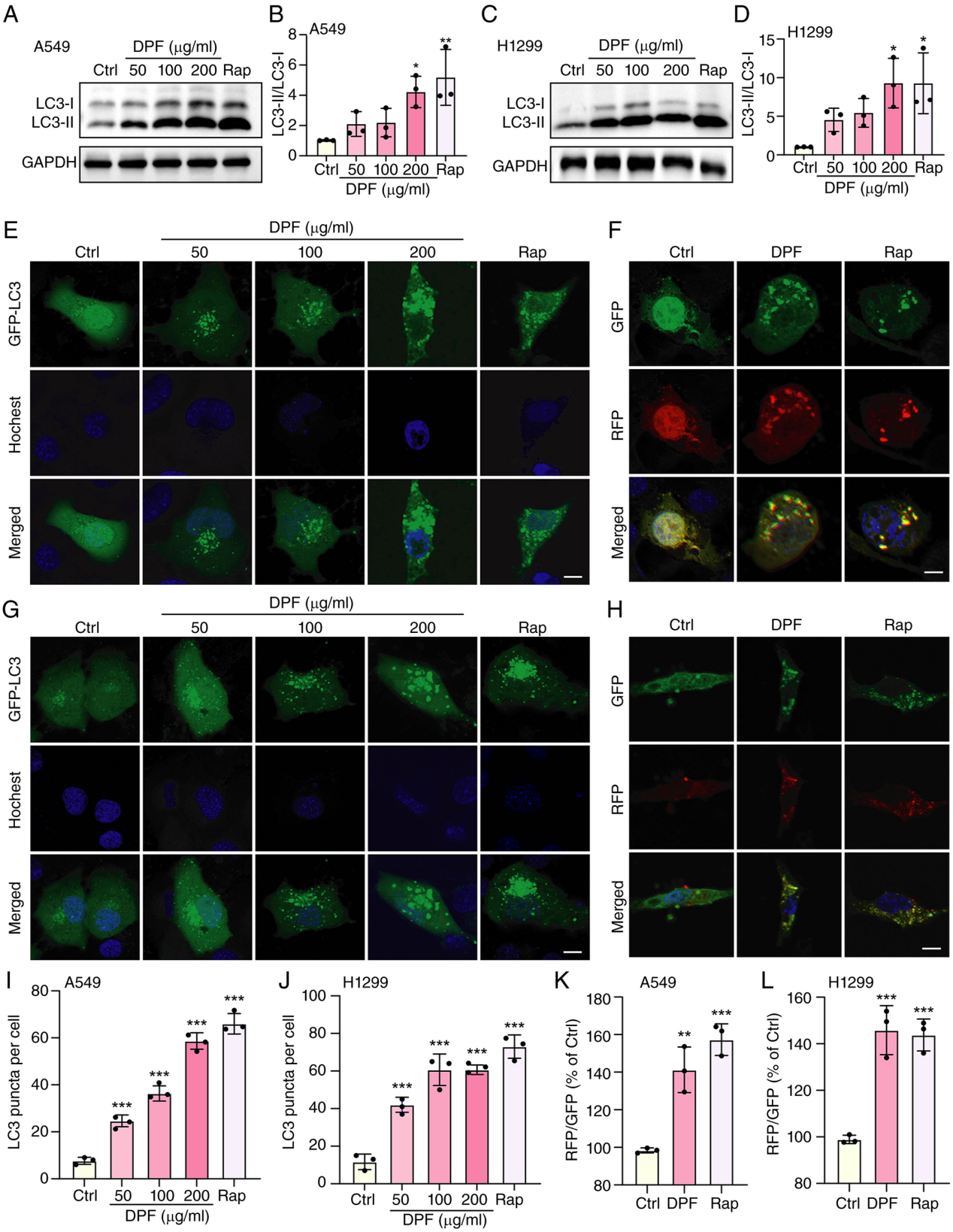


Figure 4. (A) Western blotting analysis of LC3-II/LC3-I ratios in A549 cells treated with DPF at the indicated concentrations, with Rap serving as a positive control. (B) Quantification of LC3-II/LC3-I ratios in A549 cells following DPF treatment. (C) Western blotting analysis of LC3-II/LC3-I ratios in H1299 cells treated with DPF at the indicated concentrations, with Rap serving as a positive control. (D) Quantification of LC3-II/LC3-I ratios in H1299 cells following DPF treatment. (E-H) Representative fluorescence images of GFP-LC3-expressing (E) A549 and (G) H1299 cells, and tandem monomeric RFP-GFP-LC3 reporter-expressing (F) A549 and (H) H1299 cells treated with DPF or Rap; nuclei were stained with Hoechst 33342 (magnification, x63; scale bars, 20 μm). (I and J) Quantification of GFP-LC3 puncta per cell in (I) A549 and (J) H1299 cells. (K and L) Quantification of RFP/GFP ratios in (K) A549 and (L) H1299 cells, indicating changes in autophagic flux. Statistical significance is denoted as *P<0.05, **P<0.01 and ***P<0.001. Data are presented as the mean ± SD of three independent experiments. DPF, *Disporum cantoniense* petroleum ether fraction; NSCLC, non-small cell lung cancer; Rap, rapamycin; GFP, green fluorescent protein; RFP, red fluorescent protein; Ctrl, vehicle.

flux. Given that autophagy initiation is tightly controlled by upstream kinase signaling, the present study next examined whether DPF affects key pathways involved in autophagy regulation. Western blotting analysis showed that DPF significantly increased AMPK phosphorylation at 200 μg/ml in both A549 and H1299 cells (P<0.05) and significantly decreased mTOR phosphorylation at 200 μg/ml in both A549 and H1299 cell lines (P<0.05) (Fig. 5A-H). DPF also significantly increased ULK1 phosphorylation at Ser555 in A549 cells at 200 μg/ml (P<0.05). In addition, ULK1 phosphorylation at Ser757 was significantly decreased in A549 cells at 200 μg/ml (P<0.05) and in H1299 cells at 100 μg/ml (P<0.05) and 200 μg/ml (P<0.001) (Fig. 5A-J). These results suggest that DPF activates the AMPK/mTOR/ULK1 signaling pathway.

To further verify the involvement of ULK1 in DPF-induced autophagy, cells were co-treated with the ULK1 inhibitor ULK101. As shown in Fig. S3, co-treatment with ULK101 significantly attenuated the DPF-induced increase in LC3-II levels and significantly reduced the LC3-II/LC3-I ratio compared with DPF treatment alone in both A549 and H1299 cells (both P<0.05), further demonstrating that ULK1 activation is required for the autophagic response triggered by DPF. Given that previous studies have implicated the MEK/ERK pathway in the regulation of autophagy, the present study next examined whether this pathway was activated in response to DPF treatment. As shown in Fig. 5K-P, DPF significantly increased ERK phosphorylation in A549 cells at 50, 100 and 200 μg/ml (all P<0.05) and in H1299 cells at 200 μg/ml (P<0.05). MEK phosphorylation was significantly increased at 200 μg/ml in both A549 and H1299 cells (both P<0.01), indicating activation of the MEK/ERK signaling pathway. Finally, to determine whether these signaling events contribute functionally to DPF-induced autophagy, GFP-LC3 puncta formation was examined in the presence of specific pharmacological inhibitors. Co-treatment with the AMPK inhibitor CC, the ULK1 inhibitor ULK101, or the ERK inhibitor SCH significantly reduced DPF-induced GFP-LC3 puncta formation in A549 cells compared with DPF treatment alone (Fig. 5Q and R). These findings indicate that AMPK, ULK1, and ERK signaling are implicated in the autophagic response triggered by DPF. Notably, molecular docking analysis of BBG-D, a chemical constituent of DPF, provided additional support for the involvement of upstream kinase targets. As shown in Fig. S4, BBG-D could be stably accommodated within the binding pockets of AMPK and MEK, forming favorable interactions with key amino acid residues. These *in silico* results are consistent with the experimental findings showing activation of the AMPK/mTOR/ULK1 and MEK/ERK pathways by DPF and suggest that BBG-D may contribute, at least in part, to the autophagy-inducing activity of DPF. Collectively, these results demonstrate that DPF activates autophagy and promotes autophagic flux in NSCLC cells through coordinated regulation of the AMPK/mTOR/ULK1 and MEK/ERK signaling pathways.

DPF induces apoptosis in NSCLC cells. To determine whether DPF-mediated growth suppression involves apoptotic cell death, the present study evaluated apoptosis in NSCLC cells using flow cytometry, apoptotic protein analysis and caspase-3 activation assays. Annexin V-FITC/PI staining showed that DPF significantly increased the proportion of apoptotic cells in both A549 and H1299 cells in a concentration-dependent manner (Fig. 6A-C). To further assess the contribution of apoptosis to DPF-induced cytotoxicity, A549 cells were co-treated with the pan-caspase inhibitor ZVF. As shown in Fig. S5, co-treatment with the apoptosis inhibitor ZVF significantly increased cell viability compared with DPF treatment alone (P<0.01), indicating that apoptosis contributes, at least in part, to the growth-inhibitory effect of DPF. To examine the dependence on pro-apoptotic regulators, DPF was further tested in Bax-Bak DKO and WT MEF cells. The knockout efficiency of Bax was determined through western blotting (Fig. S6). DPF significantly decreased cell viability in WT MEF cells at 100 and 200 μg/ml (both P<0.001), whereas a significant reduction in cell viability in Bax-Bak DKO MEF cells was observed only at 200 μg/ml (P<0.001) (Fig. 6D and E). This differential response suggests that Bax-Bak DKO MEF cells are less sensitive to DPF-induced cytotoxicity, supporting the involvement of Bax/Bak-dependent apoptotic signaling in DPF-induced cell death. In addition, western blotting analysis showed that DPF significantly decreased the Bcl-2/Bax ratio in A549 cells at 100 μg/ml (P<0.05) and 200 μg/ml (P<0.01), whereas a significant decrease in H1299 cells was observed only at 200 μg/ml (P<0.05). The cleaved caspase-3/caspase-3 ratio was significantly increased in A549 cells at 50 and 100 μg/ml (both P<0.05) and in H1299 cells at 50 μg/ml (P<0.05), 100 μg/ml (P<0.01) and 200 μg/ml (P<0.05) (Fig. 6F-K). Furthermore, fluorescence staining of caspase-3 determined that DPF significantly increased caspase-3 fluorescence intensity in A549 cells in a dose-dependent manner (Fig. 6L and M). Collectively, these results demonstrate that DPF induces apoptosis in NSCLC cells, and that its cytotoxic effect is at least partially mediated through a caspase-dependent apoptotic pathway.

DPF exacerbates autophagy to induce apoptosis in A549 cells. To determine whether autophagy contributes to the cytotoxic effect of DPF, A549 cell viability was first assessed in the presence of pharmacological inhibitors targeting autophagy and its upstream regulatory pathways. Co-treatment with the autophagy inhibitor 3-MA significantly increased cell viability compared with DPF treatment alone at 1.3 mM (P<0.05), 2.5 mM (P<0.01), and 5 mM (P<0.05) (Fig. 7A). A similar protective effect was observed after chloroquine (CQ) co-treatment (Fig. S7), indicating that blockade of autophagy attenuates DPF-induced cytotoxicity. These results suggest that autophagy is functionally involved in the growth-inhibitory effect of DPF rather than serving as a protective response. To further investigate whether the signaling pathways activated by DPF participate in this process, cells were co-treated with inhibitors of AMPK, ULK1, or ERK. Inhibition of AMPK with CC significantly restored cell viability in DPF-treated A549 cells at 1.3 μM (P<0.01), 2.5 μM (P<0.001) and 5 μM (P<0.001). Similarly, inhibition of ULK1 with ULK101 significantly increased cell viability at 2.5 μM (P<0.05), 5 μM (P<0.05) and 10 μM (P<0.001), whereas inhibition of ERK with SCH significantly increased cell viability at 10 μM (P<0.05) and 20 μM (P<0.01) (Fig. 7B-D). Thus, activation of the AMPK/mTOR/ULK1 and MEK/ERK signaling pathways contributes to DPF-induced cytotoxicity through autophagy regulation. The present study next examined

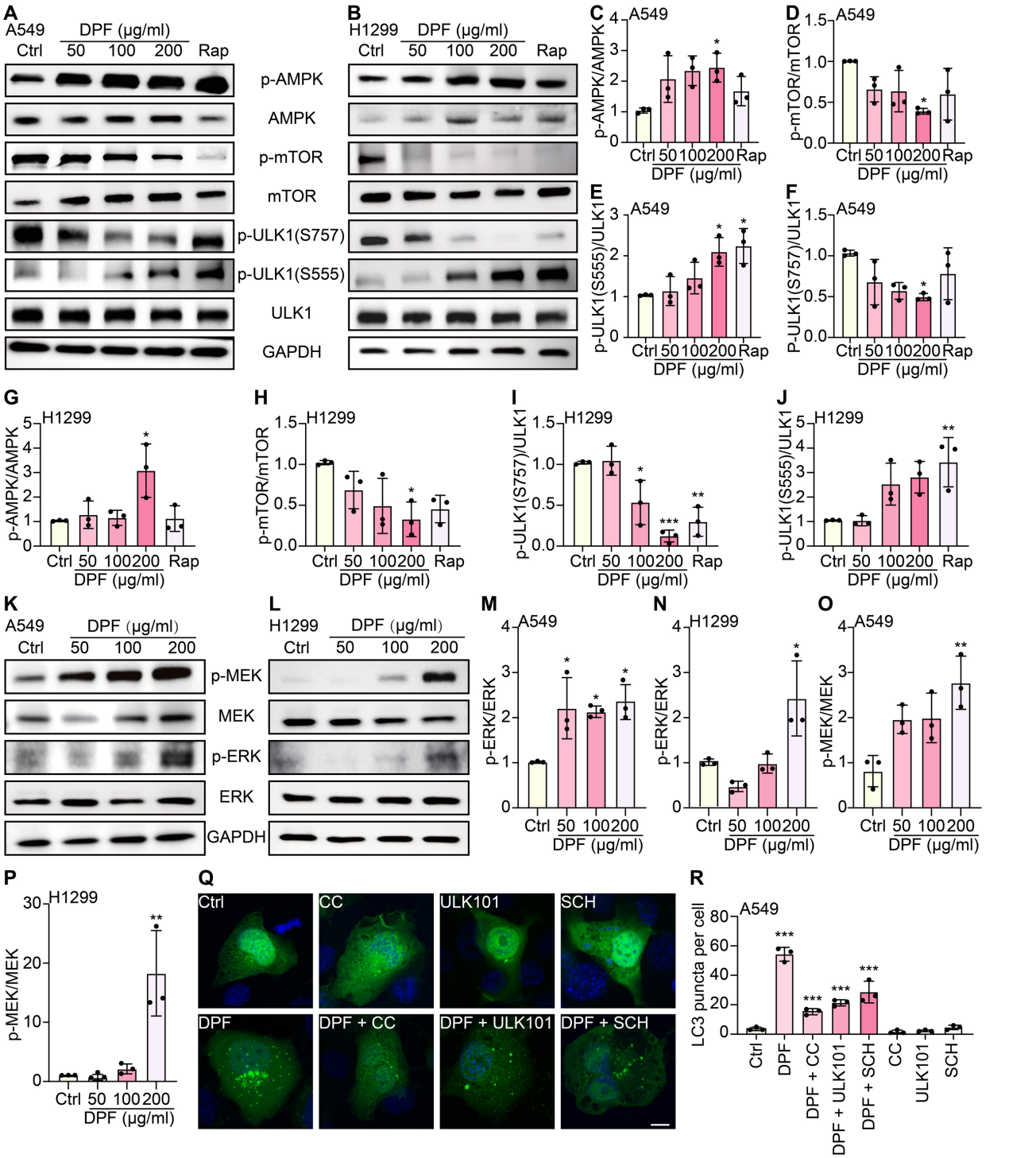


Figure 5. DPF activates autophagy in NSCLC cells through AMPK/mTOR/ULK1 and MEK/ERK pathways. (A and B) Western blotting analysis of phosphorylated and total AMPK, mTOR and ULK1 proteins in (A) A549 and (B) H1299 cells treated with DPF at the indicated concentrations, with Rap serving as a positive control. (C-J) Quantification of (C and G) p-AMPK/AMPK, (D and H) p-mTOR/mTOR, (E and J) p-ULK1(S555)/ULK1 and (F and I) p-ULK1(S757)/ULK1 in A549 and H1299 cells. (K and L) Western blotting analysis of phosphorylated and total MEK and ERK in (K) A549 and (L) H1299 cells treated with DPF. (M-P) Quantification of (M and N) p-ERK/ERK and (O and P) p-MEK/MEK in A549 and H1299 cells. (Q) Representative fluorescence images of GFP-LC3 puncta in A549 cells treated under the following conditions: Ctrl, DPF alone, CC, ULK101, SCH and their combinations with DPF. Hoechst was used to stain nuclei (magnification, x63; scale bar, 20 μm). (R) Quantification of GFP-LC3 puncta per cell in A549 cells under the indicated treatments. Statistical significance is denoted as *P<0.05, **P<0.01 and ***P<0.001. Data are presented as the mean ± SD of three independent experiments. DPF, *Disporum cantoniense* petroleum ether fraction; NSCLC, non-small cell lung cancer; Rap, rapamycin; GFP, green fluorescent protein; p-, phosphorylated; Ctrl, vehicle; CC, compound C; SCH, SCH772984; ULK1, unc-51 like autophagy activating kinase 1.

whether autophagy activation was associated with apoptosis in DPF-treated cells. Caspase-3 fluorescence staining showed that DPF significantly increased caspase-3 activation compared with the control group (P<0.001). By contrast, co-treatment with 3-MA, CC, ULK101 or SCH significantly attenuated caspase-3 activation compared with DPF treatment alone (all

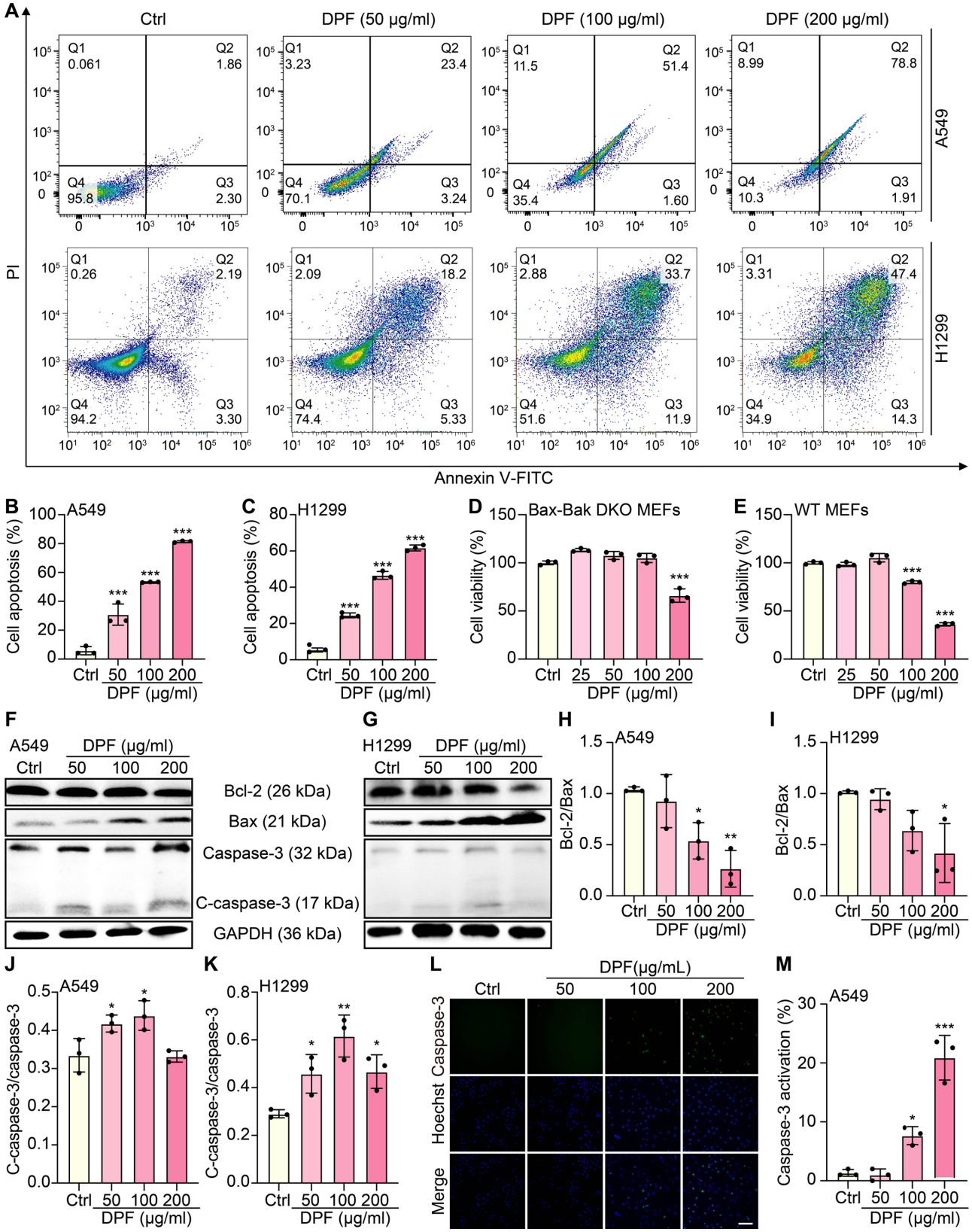


Figure 6. DPF induces apoptosis in NSCLC cells. (A) Representative flow cytometry plots showing Annexin V-FITC/PI staining in A549 and H1299 cells treated with increasing concentrations of DPF. (B and C) Quantification of total apoptotic cells in (B) A549 and (C) H1299 cells after DPF treatment. Total apoptotic cells were calculated as the sum of early and late apoptotic populations. (D and E) Cell viability of (D) Bax-Bak DKO and (E) WT MEF cells treated with DPF at the indicated concentrations. (F and G) Western blotting analysis of Bcl-2, Bax and caspase-3 in (F) A549 and (G) H1299 cells following DPF treatment. GAPDH was used as the loading control. (H and I) Quantification of the Bcl-2/Bax ratio in (H) A549 and (I) H1299 cells. (J and K) Quantification of c-caspase-3/caspase-3 levels in (J) A549 and (K) H1299 cells. (L) Representative fluorescence images of caspase-3 activation in A549 cells treated with different concentrations of DPF. Nuclei were counterstained with Hoechst (scale bar, 200 μm). (M) Quantification of caspase-3 activation (%) in A549 cells. Statistical significance is denoted as *P<0.05, **P<0.01 and ***P<0.001. Data are presented as the mean ± SD of three independent experiments. DPF, *Disporum cantoniense* petroleum ether fraction; NSCLC, non-small cell lung cancer; DKO, double knockout; WT, wild type; MEF, mouse embryonic fibroblast; PI, propidium iodide; Ctrl, vehicle; c-caspase, cleaved caspase.

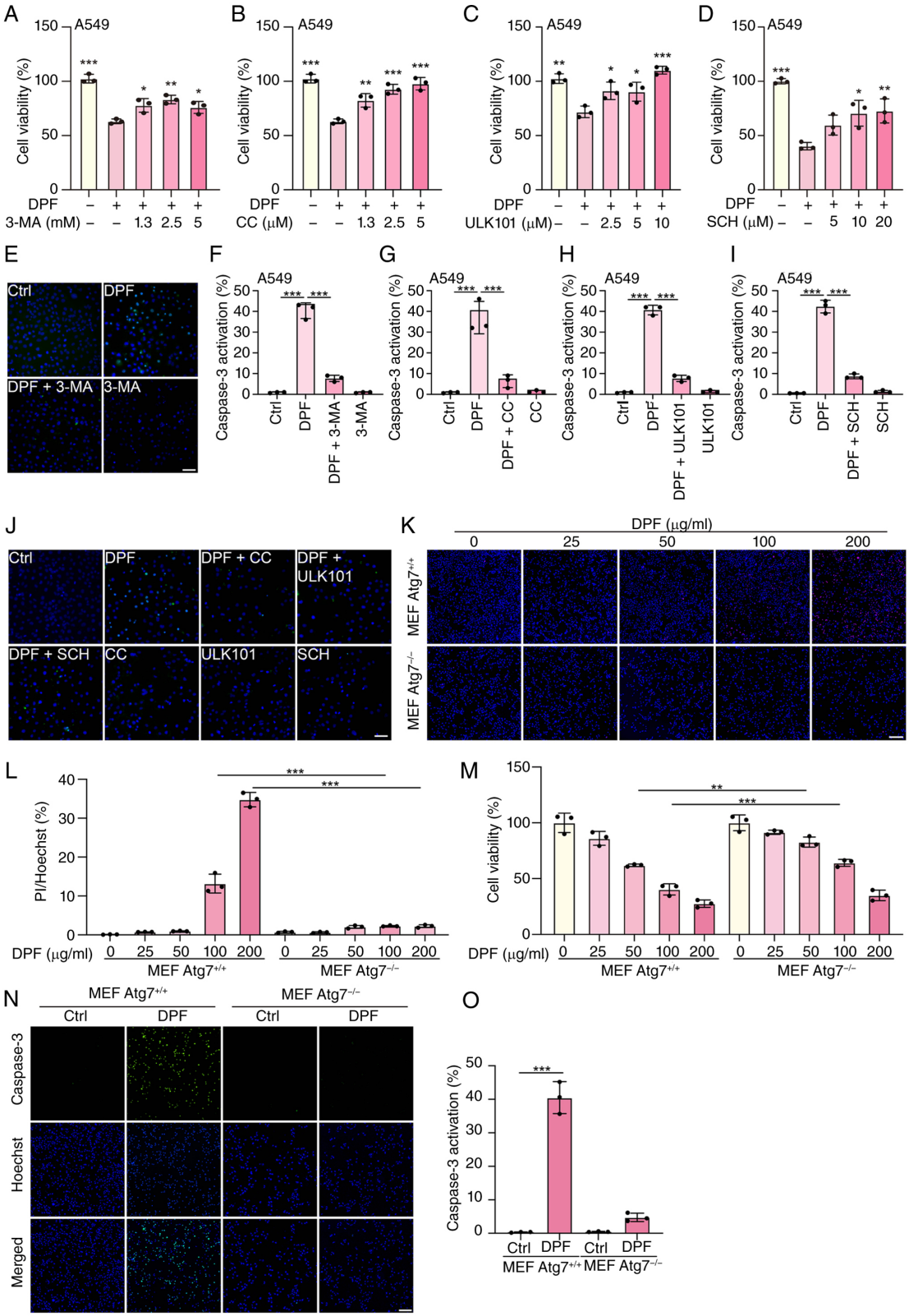


Figure 7. DPF-induced autophagy promotes apoptotic cell death. (A-D) Cell viability of A549 cells treated with DPF alone or in combination with (A) the autophagy inhibitor 3-MA, (B) AMPK inhibitor CC, (C) ULK1 inhibitor ULK101 or (D) ERK inhibitor SCH at the indicated concentrations. (E) Representative fluorescence images of caspase-3 activation in A549 cells treated with DPF, 3-MA or their combination. Nuclei were counterstained with Hoechst (scale bar, 200 μm). (F-I) Quantification of caspase-3 activation (%) in A549 cells corresponding to panels E and J. (J) Representative fluorescence images of caspase-3 activation in A549 cells treated with DPF alone or in combination with CC, ULK101 or SCH (scale bar, 200 μm). (K) Representative Hoechst/PI staining images of Atg7$^{+/+}$ and Atg7$^{-/-}$ MEF cells treated with different concentrations of DPF (scale bar, 200 μm). (L) Quantification of PI-positive cell death in Atg7$^{+/+}$ and Atg7$^{-/-}$ MEF cells after DPF treatment. (M) Cell viability of Atg7$^{+/+}$ and Atg7$^{-/-}$ MEF cells treated with DPF at the indicated concentrations. (N) Representative fluorescence images of caspase-3 activation in Atg7$^{+/+}$ and Atg7$^{-/-}$ MEF cells treated with DPF. Nuclei were counterstained with Hoechst (scale bar, 200 μm). (O) Quantification of caspase-3 activation (%) in Atg7$^{+/+}$ and Atg7$^{-/-}$ MEF cells. Statistical significance is denoted as *P<0.05, **P<0.01 and ***P<0.001. Data are presented as the means ± SD of three independent experiments. DPF, *Disporum cantoniense* petroleum ether fraction; 3-MA, 3-methyladenine; CC, compound C; ULK1, unc-51 like autophagy activating kinase 1; SCH, SCH772984; MEF, mouse embryonic fibroblast; PI, propidium iodide; Ctrl, vehicle.

P<0.001) (Fig. 7E-J). These findings indicate that inhibition of autophagy or its upstream regulatory pathways weakens DPF-induced apoptotic signaling.

To provide genetic evidence for the requirement of autophagy, the response to DPF in $Atg7^{+/+}$ and $Atg7^{-/-}$ MEF cells was further compared. The knockout efficiency of Atg7 was determined through western blotting (Fig. S8). DPF induced a concentration-dependent increase in PI-positive cell death in $Atg7^{+/+}$ MEF cells, whereas this effect was significantly attenuated in $Atg7^{-/-}$ MEF cells (Fig. 7K and L). Consistently, DPF reduced cell viability in both cell types, but $Atg7^{-/-}$ MEF cells showed significantly lower sensitivity to DPF-induced cytotoxicity compared with $Atg7^{+/+}$ MEF cells (Fig. 7M). In addition, DPF significantly increased caspase-3 activation in $Atg7^{+/+}$ MEF cells compared with the corresponding control (P<0.001), whereas no significant increase in caspase-3 activation was observed in $Atg7^{-/-}$ MEF cells following DPF treatment (Fig. 7N and O). Given that ATG7 is key in autophagosome formation, these genetic data indicate that an intact autophagy machinery is required for the full apoptotic response induced by DPF. Collectively, these pharmacological and genetic results demonstrate that DPF-induced autophagy promotes apoptotic cell death.

DPF suppresses tumor growth in A549-tumor-bearing mice. To evaluate the antitumor activity of DPF *in vivo*, an A549 xenograft mouse model was established and treated with vehicle, Gefi, or different doses of DPF. Representative images of excised tumors show that DPF treatment markedly reduced tumor size compared with the vehicle group (Fig. 8A). Consistently, longitudinal monitoring showed that DPF progressively suppressed tumor growth. Significant inhibition was observed in the 40 mg/kg DPF group on day 11 (P<0.01) and on days 13 and 15 (P<0.001), whereas the 80 mg/kg DPF group showed significant inhibition on days 11, 13 and 15 (all P<0.001). Gefi treatment also significantly inhibited tumor growth on days 11, 13 and 15 (all P<0.001) (Fig. 8B). At the end of the experiment, tumor weights were also found to be lower in the DPF-treated groups compared with the vehicle group (Fig. 8C). These findings demonstrate that DPF effectively inhibits A549 xenograft growth *in vivo*.

To further assess the *in vivo* safety of DPF, body weight and major organ weights were examined during treatment. No significant differences in body weight were observed among the groups throughout the experimental period (Fig. 8D). In addition, the weights of major organs, including the heart, liver, spleen, lung and kidney, were not significantly altered by DPF treatment (Fig. 8E). These results suggest that DPF suppresses tumor growth without causing obvious systemic toxicity. Histopathological analysis was then performed to characterize treatment-associated changes in tumor tissues. H&E staining revealed evident structural alterations in tumors from DPF-treated mice compared with the vehicle group, indicating notable tissue damage after treatment. In addition, TUNEL staining exhibited a marked increase in apoptotic signals in DPF-treated tumors (Fig. 8F), indicating that apoptosis contributes to the antitumor effect of DPF *in vivo*. To further explore the underlying mechanism, immunohistochemical staining was performed for apoptosis- and autophagy-associated markers. Compared with the vehicle group, DPF treatment significantly decreased mTOR expression at 40 mg/kg (P<0.05) and 80 mg/kg (P<0.001). DPF also significantly increased ERK expression at 40 and 80 mg/kg (both P<0.001), LC3 expression at 40 and 80 mg/kg (both P<0.001), and Bax expression at 40 mg/kg (P<0.05) and 80 mg/kg (P<0.001) (Fig. 8G-K). These changes were broadly consistent with the *in vitro* findings and suggest that DPF-induced tumor suppression is associated with apoptosis- and autophagy-associated signaling changes *in vivo*. Collectively, these results indicate that DPF exerts antitumor activity in A549 xenograft mice without evident systemic toxicity.

Discussion

NSCLC remains a predominant subtype of lung cancer and continues to account for a notable proportion of cancer-associated mortality worldwide, despite marked advances in targeted therapy and immunotherapy (1). A key obstacle to durable therapeutic benefit is the persistence of aggressive cellular phenotypes, including sustained proliferation, migration, invasion and resistance to cell death (10,49). In this context, the identification of bioactive natural products that suppress multiple malignant traits at once remains of marked translational interest (21,50).

In the present study, *Disporum cantoniense* was identified as a natural source with preferential inhibitory activity against NSCLC cells, and its DPF was further shown to exert broad antitumor effects by reducing viability, proliferation, clonogenicity, migration and invasion, while displaying weaker cytotoxicity in BEAS-2B cells. This preferential activity toward malignant cells is noteworthy because the therapeutic value of natural product-derived candidates depends not only on cytotoxic potency but also on their ability to distinguish tumor cells from non-malignant epithelial counterparts (21). In addition to suppressing cell viability, DPF increased LDH release and PI-positive staining in NSCLC cells, indicating that the viability loss was accompanied by membrane-damaging cytotoxicity rather than reflecting reduced metabolic activity. Previous phytochemical work regarding *Disporum cantoniense* has mainly focused on compound isolation and anti-inflammatory activity, whereas its antitumor potential has remained largely unexplored (22). Therefore, the present findings extend the pharmacological effects of this medicinal plant and position DPF as the principal bioactive fraction.

Mechanistically, the present data support a model in which DPF suppresses NSCLC growth through coordinated induction of autophagy and apoptosis. This interpretation is consistent with the well-established crosstalk between autophagy and apoptosis, two tightly coordinated stress-response programs that shape the balance between tumor cell survival and death under cytotoxic conditions (51-53). In NSCLC, autophagy is considered a context-dependent process that may either sustain tumor cell survival under stress or promote cell death when excessively activated or prolonged (54-56). The present inhibitor experiments favor the latter interpretation, as blockade of autophagy with 3-MA or CQ partially rescued viability and attenuated caspase-3 activation. These findings indicate that DPF-triggered autophagy is not merely an adaptive response but instead functions as a pro-death mechanism that amplifies apoptotic execution. Notably, this conclusion was further strengthened by genetic evidence using $Atg7^{+/+}$

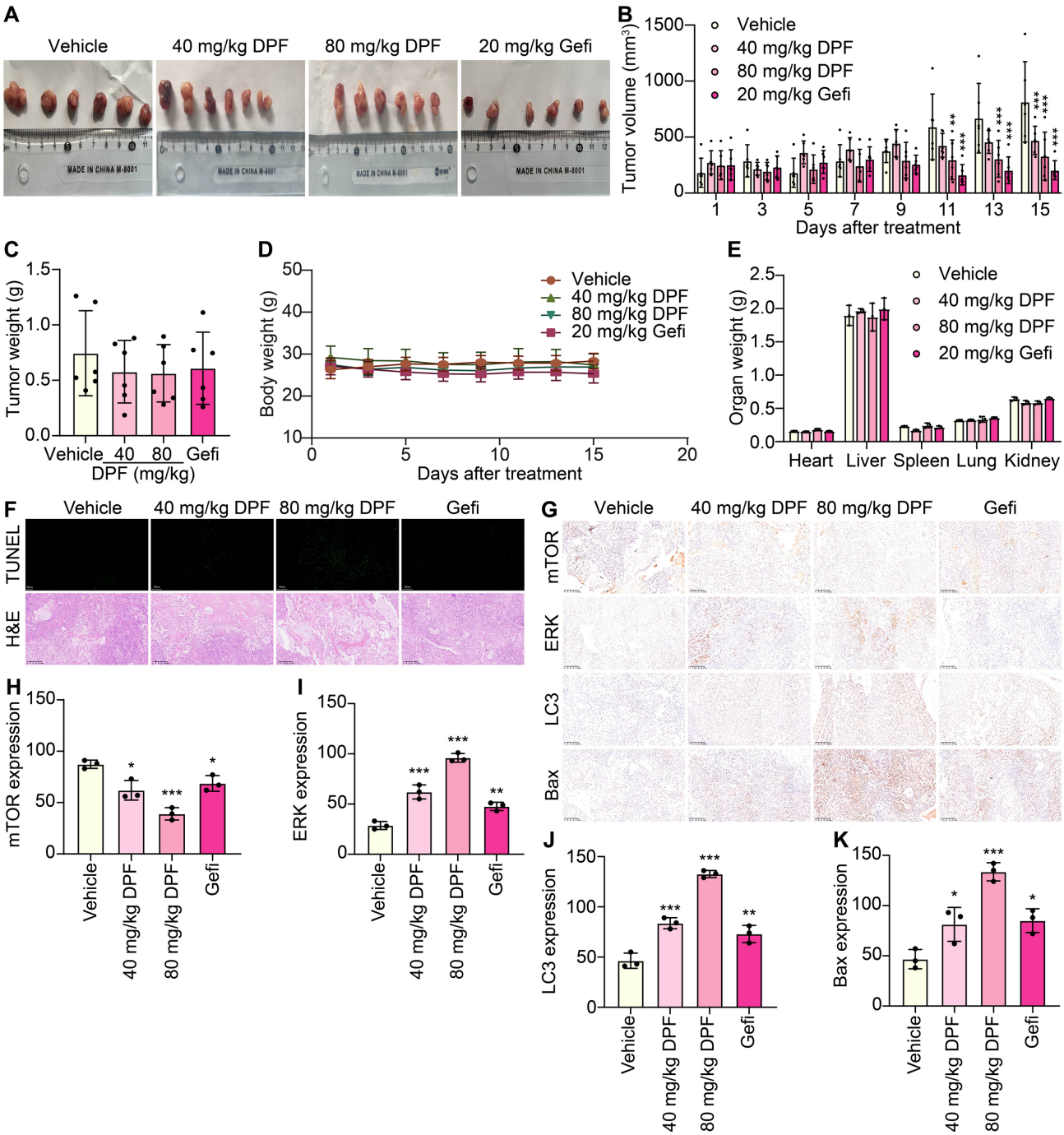


Figure 8. DPF suppresses tumor growth in A549 xenograft mice. (A) Representative images of excised tumors from mice treated with vehicle, Gefi (20 mg/kg) or DPF (40 and 80 mg/kg). (B) Tumor growth curves of A549 xenograft mice in different treatment groups. (C) Final tumor weights in mice treated with vehicle, Gefi or DPF at the indicated doses. (D) Body weight changes of mice during the treatment period. (E) Organ weights of the heart, liver, spleen, lung and kidney in each group. (F) Representative H&E and TUNEL staining images of tumor tissues from mice treated with vehicle, DPF (40 or 80 mg/kg) or Gefi (magnification, x10; scale bar, 200 μm). (G) Representative immunohistochemical staining images of mTOR, ERK, LC3 and Bax in tumor tissues from each group (magnification, x10; scale bar, 200 μm). (H-K) Quantitative analysis of (H) mTOR, (I) ERK, (J) LC3 and (K) Bax expression based on immunohistochemical staining. Statistical significance is indicated as *P<0.05, **P<0.01 and ***P<0.001. Data are presented as the mean ± SD. n=6 mice per group for tumor growth, tumor weight, body weight and organ weight analyses. DPF, *Disporum cantoniense* petroleum ether fraction; Gefi, gefitinib.

and Atg7$^{-/-}$ MEF cells. Compared with Atg7$^{+/+}$ MEF cells, Atg7$^{-/-}$ MEF cells exhibited reduced PI-positive cell death, attenuated viability loss and lower caspase-3 activation after DPF treatment. Given that ATG7 is required for autophagosome formation, the reduced response in Atg7-deficient cells indicates that the autophagy machinery contributes functionally to DPF-induced apoptosis. These results aid in addressing the limitation of relying solely on pharmacological inhibitors and provide independent genetic support for autophagy-dependent apoptosis. Therefore, distinguishing protective autophagy from pro-death autophagy is key in interpreting the biological consequence of DPF-induced autophagic flux. In the present study, a number of lines of evidence support the latter interpretation. First, DPF increased LC3-II accumulation, GFP-LC3

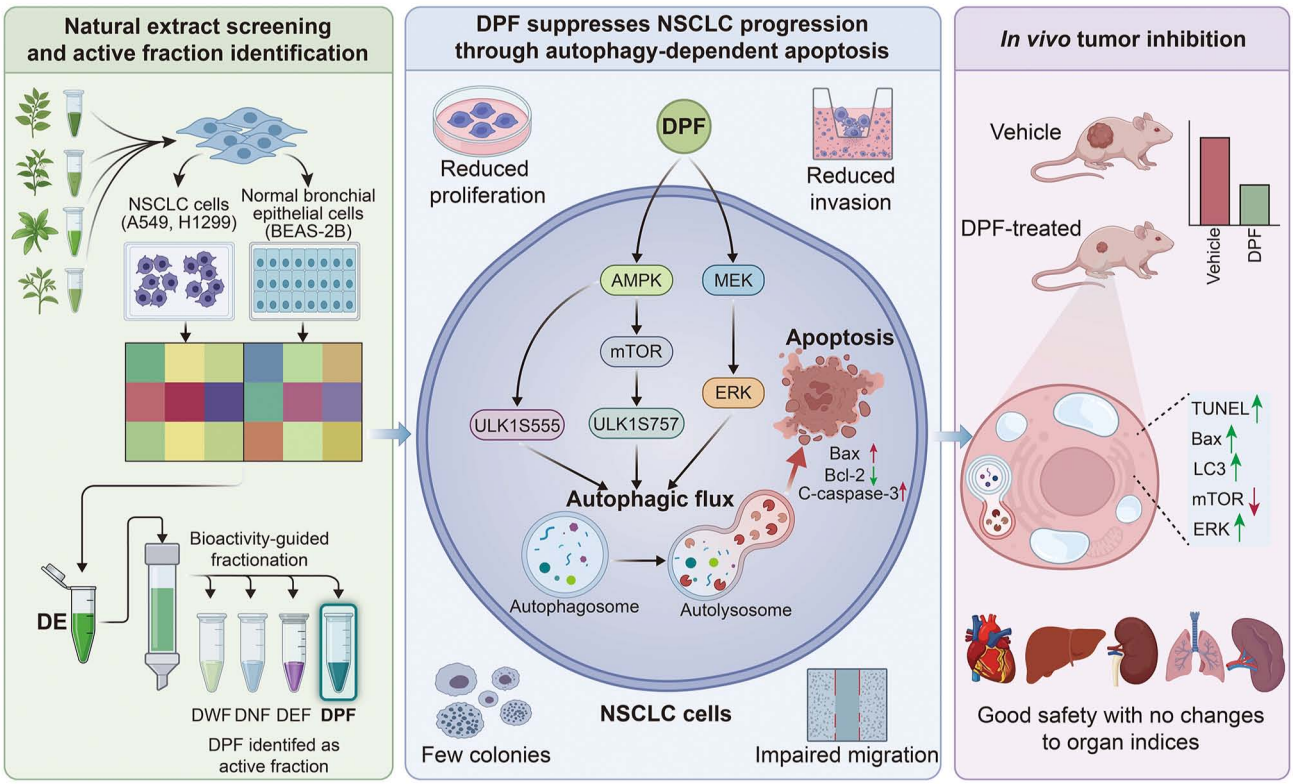


Figure 9. Schematic summary of the anti-NSCLC effects and underlying mechanism of DPF derived from *Disporum cantoniense*. DPF, the active fraction isolated from *Disporum cantoniense*, suppresses NSCLC cell proliferation, migration, invasion and colony formation and induces membrane-damaging cytotoxicity. Mechanistically, DPF activates AMPK/mTOR/ULK1 and MEK/ERK signaling to promote pro-death autophagic flux, which subsequently facilitates Bax/Bak- and caspase-3-dependent apoptosis. *In vivo*, DPF inhibits xenograft tumor growth without evident systemic toxicity. DE, *Disporum cantoniense* extract; DEF, *Disporum cantoniense* ethyl acetate fraction; DNF, *Disporum cantoniense* n-butanol fraction; DPF, *Disporum cantoniense* petroleum ether fraction; DWF, *Disporum cantoniense* aqueous fraction; NSCLC, non-small cell lung cancer; ULK1, unc-51 like autophagy activating kinase 1; c-caspase, cleaved caspase.

puncta formation and tandem mRFP-GFP-LC3 flux signals, indicating that DPF did not just block autophagosome degradation but promoted autophagic flux. Second, inhibition of autophagy with 3-MA or CQ partially restored cell viability and attenuated caspase-3 activation in DPF-treated cells. If DPF-induced autophagy primarily served as a cytoprotective response, autophagy blockade would be expected to aggravate, rather than alleviate, DPF-induced cytotoxicity. Third, inhibition of upstream autophagy regulators, including AMPK, ULK1 and ERK, also reduced DPF-induced cytotoxicity and caspase-3 activation. These findings indicate that autophagy is functionally required for the full apoptotic response induced by DPF, which is consistent with the concept of autophagy-dependent or autophagy-mediated cell death (57,58).

Furthermore, the present study suggests that this cytotoxic autophagic program is mediated, at least in part, through the AMPK/mTOR/ULK1 axis. The observed increase in AMPK phosphorylation, decrease in mTOR phosphorylation, elevation of ULK1 Ser555 phosphorylation and reduction in ULK1 Ser757 phosphorylation are consistent with a canonical autophagy-activating state. Foundational work established that AMPK and mTOR converge on ULK1 to regulate autophagy initiation, with mTOR-dependent phosphorylation of ULK1 at Ser757 disrupting AMPK/ULK1 interaction, whereas AMPK-dependent phosphorylation activates the autophagic machinery (56,59). Despite subsequent work having revealed context-dependent complexity in AMPK/ULK1 regulation (60,61), the signaling pattern observed in the present study, together with the reversal by CC and ULK101, supports the conclusion that DPF engages an upstream kinase network that favors autophagy initiation.

In addition to AMPK/mTOR/ULK1 signaling, the present data indicate that MEK/ERK acts as another upstream regulatory branch involved in DPF-induced autophagy-dependent apoptosis. ERK signaling is classically associated with proliferation and survival in lung cancer but sustained or context-specific ERK activation can also contribute to apoptosis, autophagy, senescence or growth suppression (62-64). In the present study, DPF increased MEK and ERK phosphorylation, whereas pharmacological ERK inhibition reduced GFP-LC3 puncta formation, restored cell viability and weakened caspase-3 activation. These findings suggest that MEK/ERK signaling is not just a parallel stress response but functionally participates in the autophagic and apoptotic effects of DPF. Therefore, AMPK/mTOR/ULK1 and MEK/ERK may represent two coordinated upstream signaling branches that converge on autophagy induction. The AMPK/mTOR/ULK1 axis primarily supports autophagy initiation, while MEK/ERK signaling may further amplify or sustain the autophagic response under DPF treatment. The attenuation of caspase-3 activation by inhibitors targeting either branch places apoptosis downstream, at least in part, of DPF-induced autophagy.

The present apoptosis data are also consistent with activation of the intrinsic mitochondrial pathway. DPF increased Annexin V positivity, elevated cleaved caspase-3, increased

Bax expression and reduced Bcl-2 expression, while Bax-Bak deficiency markedly blunted cytotoxicity. These observations support a mechanism in which DPF shifts the Bcl-2 family balance toward mitochondrial outer membrane permeabilization and caspase-dependent apoptosis. Notably, the attenuation of caspase-3 activation by autophagy and pathway inhibitors places apoptosis downstream, at least in part, of the autophagic response (51,55,65). Thus, DPF-induced autophagy and apoptosis should not be viewed as two independent events. Instead, the present data support a mechanistic sequence in which DPF activates AMPK/mTOR/ULK1 and MEK/ERK signaling, promotes pro-death autophagic flux and subsequently facilitates Bax/Bak- and caspase-3-dependent apoptotic execution.

Beyond growth inhibition, DPF also impaired migration and invasion, which are clinically relevant features because metastatic dissemination remains a primary cause of cancer-associated mortality. The transcriptomic enrichment of pathways associated with apoptotic signaling, growth regulation, MAPK signaling and migration is therefore well aligned with the phenotypic data. Despite the present study having not dissected epithelial-mesenchymal transition or extracellular matrix remodeling in detail, the increased remaining wound area in wound-healing assays and the reduced Transwell invasion together suggest that DPF affects a broader malignant-state program rather than only inducing acute cytotoxicity. This is important because agents capable of simultaneously restraining survival and invasive behavior may exhibit greater therapeutic value than compounds acting on proliferation alone (50,66).

The present xenograft data further substantiate the *in vivo* relevance of these findings. DPF markedly reduced tumor volume and weight, increased TUNEL positivity, enhanced Bax and LC3 expression and decreased mTOR levels in tumor tissues, without evident effects on body weight or major organ weights. These changes were broadly consistent with the *in vitro* findings and suggest that DPF-induced tumor suppression is associated with apoptosis- and autophagy-associated signaling changes *in vivo*. Despite this, the safety profile should be interpreted with caution. Although no overt systemic toxicity was observed during the treatment period, these data are insufficient to define long-term safety, pharmacokinetic behavior or therapeutic index at the level of the active constituents. More comprehensive toxicological studies, plasma exposure assessments and histopathological analyses will be required to support future translational development (21,49,56).

A number of limitations should also be acknowledged. First, the active components characterized in the present study were fractions rather than purified single compounds. Despite UHPLC-Q/TOF-MS/MS having annotated 14 constituents and molecular docking having suggested that BBG-D may interact with AMPK and MEK, these *in silico* observations were hypothesis-generating rather than definitive evidence of target engagement. Future work should isolate the major constituents, determine which compound or combination is required for activity and further validate direct binding using biochemical or biophysical approaches. Second, the majority of mechanistic experiments were performed in A549 and H1299 cells; broader validation across genetically diverse NSCLC models, including EGFR-mutant, KRAS-mutant, and therapy-resistant settings, would clarify the range of responsiveness (10,49). Third, although the $Atg7^{+/+}$ and $Atg7^{-/-}$ MEF experiments provided genetic evidence that ATG7-dependent autophagy contributes to DPF-induced apoptosis, these experiments were performed in MEF cells rather than NSCLC cells. Therefore, future studies using NSCLC-specific genetic approaches, including ATG7, ATG5 or ULK1 knockdown or knockout in A549 and H1299 cells, would further strengthen the mechanistic conclusion (55,56,59). Finally, whether DPF can synergize with current NSCLC therapies such as EGFR inhibitors, chemotherapy or immunotherapy remains unknown and deserves investigation, particularly given the ongoing need to overcome resistance in advanced disease.

In conclusion, the present study identified DPF, the petroleum ether fraction of *Disporum cantoniense*, as a selective inhibitor of NSCLC progression that acts through coordinated activation of autophagy and apoptosis. The present data support that DPF regulates AMPK/mTOR/ULK1 and MEK/ERK signaling to drive autophagic flux, which in turn promotes Bax/Bak- and caspase-3-dependent apoptosis and suppresses tumor growth both *in vitro* and *in vivo* (Fig. 9). Conceptually, these findings identify *Disporum cantoniense* as a medicinal plant with anti-NSCLC potential and further support cytotoxic autophagy as a targetable vulnerability in lung cancer.

Acknowledgements

Not applicable.

Funding

The present study was supported by the Natural Science Foundation of China (grant no. 81903829), the Open Project from the State Key Laboratory of Traditional Chinese Medicine Syndrome (grant no. SKLKY2024B0006), the Foundation of Institute of Traditional Chinese Medicine Health Industry, China Academy of Chinese Medical Sciences (grant no. ZYTS-2025011), Ziyang Central Hospital-Southwest Medical University Science and Technology Strategic Cooperation (grant no. 2025ZYXNYD13), the Open Fund of Innovation Center for Basic Research on Metabolic Cardiovascular Diseases, Southwest Medical University (grant no. xnykdxcxzx-2025-10), the Joint Project of Luzhou Municipal People's Government and Southwest Medical University (grant no. 2024LZXNYDJ026), the Sichuan Provincial Central Government-Guided Local Scientific Research Project (grant no. 2025ZYD0025) and the Luzhou Science and Technology Program (grant no. 2025JBH004).

Availability of data and materials

The data generated in the present study may be found in the Genome Sequence Archive of the National Genomics Data Center under accession number HRA020513 or at the following URL: https://ngdc.cncb.ac.cn/gsa-human/browse/HRA020513.

Authors' contributions

CF and YJ were responsible for data curation and the development and establishment of the cellular and animal experimental models. RC and QC also contributed to data curation. YP, JW and DQ conducted the investigation and performed validation

experiments, including western blotting, flow cytometry and immunohistochemistry, to confirm the reproducibility of the experimental findings. DQ contributed to writing, reviewing and editing the manuscript. BYKL contributed to the experimental investigation. VKWW contributed to the development of the analytical approaches used for the transcriptomic and network pharmacology analyses. XZ, JL and AW conceptualized the present study. JL and AW were also responsible for funding acquisition, supervision, preparation of the original manuscript draft, and reviewing and editing the manuscript. CF and AW confirm the authenticity of all the raw data. All authors have read and approved the final version of the manuscript.

Ethics approval and consent to participate

All animal experiments were approved by the Institutional Animal Care and Use Committee of Southwest Medical University (Luzhou, China; approval no. 20240514-004) and performed in accordance with relevant ethical guidelines.

Patient consent for publication

Not applicable.

Competing interests

The authors declare that they have no competing interests.

References

1. Bray F, Laversanne M, Sung H, Ferlay J, Siegel RL, Soerjomataram I and Jemal A: Global cancer statistics 2022: GLOBOCAN estimates of incidence and mortality worldwide for 36 cancers in 185 countries. CA Cancer J Clin 74: 229-263, 2024.
2. Mirhadi S, Tam S, Li Q, Moghal N, Pham NA, Tong J, Golbourn BJ, Krieger JR, Taylor P, Li M, *et al*: Integrative analysis of non-small cell lung cancer patient-derived xenografts identifies distinct proteotypes associated with patient outcomes. Nat Commun 13: 1811, 2022.
3. Ye Q, Zhou L, Jin P, Li L, Zheng S, Huang Z, Liu J, Qin S, Liu H, Zou B and Xie K: Guaiazulene triggers ROS-induced apoptosis and protective autophagy in non-small cell lung cancer. Front Pharmacol 12: 621181, 2021.
4. Yang J, He X, Lv Q, Jing J and Shi H: Management of adverse events in cancer patients treated with PD-1/PD-L1 blockade: Focus on Asian populations. Front Pharmacol 10: 726, 2019.
5. Hu T, Gong H, Xu J, Huang Y, Wu F and He Z: Nanomedicines for overcoming cancer drug resistance. Pharmaceutics 14: 1606, 2022.
6. Yu L, Lai Q, Gou L, Feng J and Yang J: Opportunities and obstacles of targeted therapy and immunotherapy in small cell lung cancer. J Drug Target 29: 1-11, 2021.
7. Luan Y, Xian D, Zhao C, Qing X, He H, Zheng K, Song W, Jiang T, Wang W and Duan C: Therapeutic targets for lung cancer: Genome-wide Mendelian randomization and colocalization analyses. Front Pharmacol 15: 1441233, 2024.
8. Zhang C, Shao J, Tang X, Wu J, Li P, Li W and Wang C: The real-world treatment characteristic and efficacy of immune checkpoint inhibitors in non-small cell lung cancer: Data from a retrospective cohort study. Int Immunopharmacol 134: 112152, 2024.
9. Dong J, Li B, Lin D, Zhou Q and Huang D: Advances in targeted therapy and immunotherapy for non-small cell lung cancer based on accurate molecular typing. Front Pharmacol 10: 230, 2019.
10. Hiltbrunner S, Cords L, Kasser S, Freiberger SN, Kreutzer S, Toussaint NC, Grob L, Opitz I, Messerli M, Zoche M, *et al*: Acquired resistance to anti-PD1 therapy in patients with NSCLC associates with immunosuppressive T cell phenotype. Nat Commun 14: 5154, 2023.
11. Liang H, Xu Y, Zhao J, Chen M and Wang M: Hippo pathway in non-small cell lung cancer: Mechanisms, potential targets, and biomarkers. Cancer Gene Ther 31: 652-666, 2024.
12. Wang Y, Zhou Y, Zhou K, Li J and Che G: Prognostic value of pre-treatment red blood cell distribution width in lung cancer: A meta-analysis. Biomarkers 25: 241-247, 2020.
13. Zhang J, Ren Z, Hu Y, Shang S, Wang R, Ma J, Zhang Z, Wu M, Wang F, Yu J and Chen D: High $HPK1^{+}PD\text{-}1^{+}TIM\text{-}3^{+}CD8^{+}$ T cells infiltration predicts poor prognosis to immunotherapy in NSCLC patients. Int Immunopharmacol 127: 111363, 2024.
14. Yuan M, Huang LL, Chen JH, Wu J and Xu Q: The emerging treatment landscape of targeted therapy in non-small-cell lung cancer. Signal Transduct Target Ther 4: 61, 2019.
15. Lin Q, Qu M, Patra HK, He S, Wang L, Hu X, Xiao L, Fu Y, Gong T, He Q, *et al*: Mechanistic and therapeutic study of novel anti-tumor function of natural compound imperialine for treating non-small cell lung cancer. J Ethnopharmacol 247: 112283, 2020.
16. Lan T, He S, Luo X, Pi Z, Lai W, Jiang C, Gan J, Wei S, Wu Z, Yun C, *et al*: Disruption of NADPH homeostasis by total flavonoids from Adinandra nitida Merr. Ex Li leaves triggers ROS-dependent p53 activation leading to apoptosis in non-small cell lung cancer cells. J Ethnopharmacol 332: 118340, 2024.
17. Liu Y, Luo X, Liu J, Ma Y, Tan J, Wang W, Hu J, Fu X, Xu L, Yu F, *et al*: Shenlingcao oral liquid for patients with non-small cell lung cancer receiving adjuvant chemotherapy after radical resection: A multicenter randomized controlled trial. Phytomedicine 113: 154723, 2023.
18. Ni Y, Liu J, Zeng L, Yang Y, Liu L, Yao M, Chai L, Zhang L, Li Y, Zhang L and Li W: Natural product manoalide promotes EGFR-TKI sensitivity of lung cancer cells by KRAS-ERK pathway and mitochondrial Ca^{2+} overload-induced ferroptosis. Front Pharmacol 13: 1109822, 2023.
19. Yang S, Zhang Y, Luo Y, Xu B, Yao Y, Deng Y, Yang F, Ye T, Wang G, Cheng Z, *et al*: Hinokiflavone induces apoptosis in melanoma cells through the ROS-mitochondrial apoptotic pathway and impairs cell migration and invasion. Biomed Pharmacother 103: 101-110, 2018.
20. Zheng Y, Wang PP, Fu Y, Chen YY and Ding ZY: Zoledronic acid enhances the efficacy of immunotherapy in non-small cell lung cancer. Int Immunopharmacol 110: 109030, 2022.
21. Atanasov AG, Zotchev SB, Dirsch VM, Orhan IE, Banach M, Rollinger JM, Barreca D, Weckwerth W, Bauer R, Bayer EA, *et al*: Natural products in drug discovery: Advances and opportunities. Nat Rev Drug Discov 20: 200-216, 2021.
22. Li Z, Zhao H, Ouyang H, Wang Q, Chen J, Feng Y and Yang S: New compounds with anti-inflammatory potential from *Disporum cantoniense*. Phytochem Lett 22: 92-94, 2017.
23. Chen L, Su YF, Yin ZY, Luo XH, Wu ZH, Gao XM and Zhang BL: Flavonoids from *Disporum cantoniense* (Liliaceae). Biochem Syst Ecol 37: 609-612, 2009.
24. Panche AN, Diwan AD and Chandra SR: Flavonoids: An overview. J Nutr Sci 5: e47, 2016.
25. Yan W, Yang J, Tang H, Xue L, Chen K, Wang L, Zhao M, Tang M, Peng A, Long C, *et al*: Flavonoids from the stems of Millettia pachyloba Drake mediate cytotoxic activity through apoptosis and autophagy in cancer cells. J Adv Res 20: 117-127, 2019.
26. Lipinski CA: Lead- and drug-like compounds: The rule-of-five revolution. Drug Discov Today Technol 1: 337-341, 2004.
27. Pan Y, Wei J, Qin D, Zhou X, Gao F, Yu L, Feng C, Mi J, Wu J, Law BYK, *et al*: Prosapogenin CP4 exacerbates mitophagy to induce apoptosis via AMPK-mTOR and PINK1/Parkin pathways in A549 cells. Phytomedicine 148: 157333, 2025.
28. Yong YY, Yan L, Wang BD, Fan DS, Guo MS, Yu L, Wu JM, Qin DL, Law BYK, Wong VKW, *et al*: Penthorum chinense Pursh inhibits ferroptosis in cellular and Caenorhabditis elegans models of Alzheimer's disease. Phytomedicine 127: 155463, 2024.
29. Qiu WQ, Ai W, Zhu FD, Zhang Y, Guo MS, Law BYK, Wu JM, Wong VKW, Tang Y, Yu L, *et al*: Polygala saponins inhibit NLRP3 inflammasome-mediated neuroinflammation via SHP-2-mediated mitophagy. Free Radic Biol Med 179: 76-94, 2022.
30. Qiu WQ, Yu L, He CL, Wu JM, Law BYK, Yu CL, Qin DL, Zhou XG and Wu AG: Two 18-norspirostane steroidal saponins as novel mitophagy enhancers improve Alzheimer's disease. Clin Transl Med 13: e1390, 2023.
31. Chen X, Zhou XY, Lan C, Fu HJ, Li ZC, Chen MY, Wen YP, Yu L, Qin DL, Wu AG, *et al*: Araloside A induces Raf/MEK/ERK-dependent autophagy to mitigate Alzheimer's and Parkinson's pathology in cellular and C. elegans models. Mol Neurobiol 62: 16061-16080, 2025.

32. Stefanowicz Hajduk J and Ochocka JR: Real-time cell analysis system in cytotoxicity applications: Usefulness and comparison with tetrazolium salt assays. Toxicol Rep 7: 335-344, 2020.
33. Justus CR, Marie MA, Sanderlin EJ and Yang LV: Transwell in vitro cell migration and invasion assays. Methods Mol Biol 2644: 349-359, 2023.
34. Teng JF, Mei QB, Zhou XG, Tang Y, Xiong R, Qiu WQ, Pan R, Law BYK, Wong VKW, Yu CL, *et al*: Polyphyllin VI induces caspase-1-mediated pyroptosis via the induction of ROS/NF-κB/NLRP3/GSDMD signal axis in non-small cell lung cancer. Cancers (Basel) 12: 193, 2020.
35. Yan H, Wang S, Hu Y, Jing R, Liu L, Liu P, Yin H and Mu L: AG8 induces apoptosis and ferroptosis through regulating caspase 3 and SLC7A11/GPX4 signaling pathway in triple-negative breast cancer. Clin Tradit Med Pharmacol 6: 200222, 2025.
36. Chen X, Xie Q, Cheng X, Diao X, Cheng Y, Liu J, Xie W, Chen Z and Zhu B: Role of interleukin-17 in lymphangiogenesis in non-small-cell lung cancer: Enhanced production of vascular endothelial growth factor C in non-small-cell lung carcinoma cells. Cancer Sci 101: 2384-2390, 2010.
37. Balikci Cicek I and Kucukakcali Z: Transcriptomic profiling of gastric cancer reveals key biomarkers and pathways via bioinformatic analysis. Genes (Basel) 16: 829, 2025.
38. Luo W, Deng J, He J, Yin L, You R, Zhang L, Shen J, Han Z, Xie F, He J and Guan Y: Integration of molecular docking, molecular dynamics and network pharmacology to explore the multi-target pharmacology of fenugreek against diabetes. J Cell Mol Med 27: 1959-1974, 2023.
39. Guo M, Wang Z, Zhou X, Yu C, Wu J, Yu L, Mi J, Ren F, Law BYK, Pan H, *et al*: Ciliatoside A attenuates neuroinflammation in Alzheimer's disease by activating mitophagy and inhibiting NLRP3 inflammasome activation. Phytomedicine 145: 156928, 2025.
40. Chang TM, Chi MC, Chiang YC, Lin CM, Fang ML, Lee CW, Liu JF and Kou YR: Promotion of ROS-mediated apoptosis, G2/M arrest, and autophagy by naringenin in non-small cell lung cancer. Int J Biol Sci 20: 1093-1109, 2024.
41. Chen C, Ou W, Yang C, Liu H, Yang T, Mo H, Lu W, Yan J and Chen A: Queen bee acid pretreatment attenuates myocardial ischemia/reperfusion injury by enhancing autophagic flux. Heliyon 10: e33371, 2024.
42. Gong Y, Luo S, Fan P, Zhu H, Li Y and Huang W: Growth hormone activates PI3K/Akt signaling and inhibits ROS accumulation and apoptosis in granulosa cells of patients with polycystic ovary syndrome. Reprod Biol Endocrinol 18: 121, 2020.
43. Dai S, Wei J, Zhang H, Luo P, Yang Y, Jiang X, Fei Z, Liang W, Jiang J and Li X: Intermittent fasting reduces neuroinflammation in intracerebral hemorrhage through the Sirt3/Nrf2/HO-1 pathway. J Neuroinflammation 19: 122, 2022.
44. Yong Y, Yan L, Wei J, Feng C, Yu L, Wu J, Guo M, Fan D, Yu C, Qin D, *et al*: A novel ferroptosis inhibitor, Thonningianin A, improves Alzheimer's disease by activating GPX4. Theranostics 14: 6161-6184, 2024.
45. Vijaya Kumar A, Donate C, Imhof BA and Matthes T: Tumor engraftment in a xenograft mouse model of human mantle cell lymphoma. J Vis Exp: 56023, 2018.
46. Tang X, Ding H, Liang M, Chen X, Yan Y, Wan N, Chen Q, Zhang J and Cao J: Curcumin induces ferroptosis in non-small-cell lung cancer via activating autophagy. Thorac Cancer 12: 1219-1230, 2021.
47. Xie C, Zhou X, Liang C, Li X, Ge M, Chen Y, Yin J, Zhu J and Zhong C: Apatinib triggers autophagic and apoptotic cell death via VEGFR2/STAT3/PD-L1 and ROS/Nrf2/p62 signaling in lung cancer. J Exp Clin Cancer Res 40: 266, 2021.
48. Zhang X, Zheng X, Ying X, Xie W, Yin Y and Wang X: CEBPG suppresses ferroptosis through transcriptional control of SLC7A11 in ovarian cancer. J Transl Med 21: 334, 2023.
49. Meyer ML, Fitzgerald BG, Paz Ares L, Cappuzzo F, Jänne PA, Peters S and Hirsch FR: New promises and challenges in the treatment of advanced non-small-cell lung cancer. Lancet 404: 803-822, 2024.
50. Yang Y, Wang H, Xue Q, Peng W and Zhou Q: New advances of natural products in non-small cell lung cancer: From mechanisms to therapies. J Ethnopharmacol 346: 119636, 2025.
51. Liu G, Pei F, Yang F, Li L, Amin AD, Liu S, Buchan JR and Cho WC: Role of autophagy and apoptosis in non-small-cell lung cancer. Int J Mol Sci 18: 367, 2017.
52. Liu H, Yao Q, Wang X, Xie H, Yang C, Gao H and Xie C: The research progress of crosstalk mechanism of autophagy and apoptosis in diabetic vascular endothelial injury. Biomed Pharmacother 170: 116072, 2024.
53. Lyu L, Hu Y, Yin S, Wang L, Ye F, Wang M, Zhou Y, Ma W, Chen C, Jiang Y, *et al*: Autophagy inhibition enhances anti-pituitary adenoma effect of tetrandrine. Phytother Res 35: 4007-4021, 2021.
54. Tang F, Zhang JN, Zhao XL, Xu LY, Ao H and Peng C: Unlocking the dual role of autophagy: A new strategy for treating lung cancer. J Pharm Anal 15: 101098, 2025.
55. Qin P, Li Q, Zu Q, Dong R and Qi Y: Natural products targeting autophagy and apoptosis in NSCLC: A novel therapeutic strategy. Front Oncol 14: 1379698, 2024.
56. Jain V, Singh MP and Amaravadi RK: Recent advances in targeting autophagy in cancer. Trends Pharmacol Sci 44: 290-302, 2023.
57. Denton D and Kumar S: Autophagy-dependent cell death. Cell Death Differ 26: 605-616, 2019.
58. Galluzzi L, Vitale I, Aaronson SA, Abrams JM, Adam D, Agostinis P, Alnemri ES, Altucci L, Amelio I, Andrews DW, *et al*: Molecular mechanisms of cell death: Recommendations of the nomenclature committee on cell death 2018. Cell Death Differ 25: 486-541, 2018.
59. Kim J, Kundu M, Viollet B and Guan KL: AMPK and mTOR regulate autophagy through direct phosphorylation of Ulk1. Nat Cell Biol 13: 132-141, 2011.
60. Wang W, Jiang J, Huang Y, Peng F, Hu T, Wu J, Pan X and Rao C: Aconitine induces autophagy via activating oxidative DNA damage-mediated AMPK/ULK1 signaling pathway in H9c2 cells. J Ethnopharmacol 282: 114631, 2022.
61. Liu X, Wu J, Wang N, Xia L, Fan S, Lu Y, Chen X, Shang S, Yang Y, Huang Q, *et al*: Artesunate reverses LPS tolerance by promoting ULK1-mediated autophagy through interference with the CaMKII-IP3R-CaMKKβ pathway. Int Immunopharmacol 87: 106863, 2020.
62. Cagnol S and Chambard JC: ERK and cell death: Mechanisms of ERK-induced cell death-apoptosis, autophagy and senescence. FEBS J 277: 2-21, 2010.
63. Huang Y, Zhen Y, Chen Y, Sui S and Zhang L: Unraveling the interplay between RAS/RAF/MEK/ERK signaling pathway and autophagy in cancer: From molecular mechanisms to targeted therapy. Biochem Pharmacol 217: 115842, 2023.
64. Timofeev O, Giron P, Lawo S, Pichler M and Noeparast M: ERK pathway agonism for cancer therapy: Evidence, insights, and a target discovery framework. NPJ Precis Oncol 8: 70, 2024.
65. Vogler M, Braun Y, Smith VM, Westhoff MA, Pereira RS, Pieper NM, Anders M, Callens M, Vervliet T, Abbas M, *et al*: The BCL2 family: From apoptosis mechanisms to new advances in targeted therapy. Signal Transduct Target Ther 10: 91, 2025.
66. Fares J, Fares MY, Khachfe HH, Salhab HA and Fares Y: Molecular principles of metastasis: A hallmark of cancer revisited. Signal Transduct Target Ther 5: 28, 2020.

Copyright © 2026 Feng et al. This work is licensed under a Creative Commons Attribution-NonCommercial-NoDerivatives 4.0 International (CC BY-NC-ND 4.0) License.